Air Quality, Atmosphere & Health (2024) 17:155–175
https://doi.org/10.1007/s11869-023-01434-w

Long-range transport and microscopy analysis of Sangay volcanic ashes in Ecuador

Daniel Moran-Zuloaga[1,2] · Wilson Merchan-Merchan[3] · Emilio Rodriguez-Caballero[4,5] · Maurizio Mulas[6] · Philip Hernick[7]

Received: 4 October 2022 / Accepted: 11 September 2023 / Published online: 4 October 2023

Abstract

This study aims to conduct a spatiotemporal analysis of the long-range transportation of volcanic ashes that originates from the eruption of the Sangay volcano and reached Guayaquil during the months of June 2020; September 2020; and April 2021. The particulate matter data ($PM_{2.5}$) was obtained using a low-cost air quality sensor. During the wet season of 2020 (Jan–May), $PM_{2.5}$ average concentrations were 6 ± 2 μg m^{-3} while during the dry season of 2020 (July–Nov), $PM_{2.5}$ average concentrations were 16 ± 3 μg m^{-3} in Guayaquil. The most prominent plumes occurred on September 20th of 2020, a month with no rain but high wind speeds created by the Andes Mountain topography to the coast. During this event, $PM_{2.5}$ concentrations started at 12:00 UTC-5 in a volcanic plume event that lasted 4 h with a maximum peak of $133 + 40$ μg m^{-3}. Electron microscopy of selected samples showed that the ashes of the three eruptions may differ in size and morphology. EDX analysis reveals that the ash contains certain elements—C, Si, Na, Mg, Al, Ca, S, and Fe—in similar proportions. In summary, this study remarks on the meteorological role and the long-range transport of Sangay volcanic ashes.

Keywords Sangay ashes · Long-range transport · Cluster analysis · Seasonality · Microscopy analysis

Abbreviations

AOD	Aerosol Optical Depth at 550 nm wavelength
CALIPSO	Cloud-Aerosol Lidar and Infrared Pathfinder Satellite Observations
FE-ESEM	Field-Emission Environmental Scanning Electron Microscope
GDAS	Global Data Assimilation System
GDLAS	Global Land Data Assimilation System
GIOVANNI	Geospatial Interactive Online Visualization and Analyze Infrastructure
HYSPLIT	Hybrid Single Particle Lagrangian Integrated Trajectory Model
IG-EPN	Instituto Geofísico de la Escuela Politécnica Nacional del Ecuador

✉ Daniel Moran-Zuloaga
dmoran@espol.edu.ec

1 Department of Chemistry, Pharmacy and Geoscience, Johannes Gutenberg University Mainz, Saarstrasse 21, 55122 Mainz, Germany

2 ESPAE Graduate School of Management, Escuela Superior Politécnica del Litoral, ESPOL, Campus Peñas, Malecón No. 100 y Loja, 090306 Guayaquil, Ecuador

3 School of Aerospace and Mechanical Engineering, University of Oklahoma, Norman, OK 73019, USA

4 Agronomy Department, University of Almeria, Almeria, Spain

5 Research Centre for Scientific Collections from the University of Almeria (CECOUAL), 04120 Almeria, Spain

6 Escuela Superior Politécnica del Litoral, ESPOL, Facultad de Ingeniería en Ciencias de la Tierra, Campus Gustavo Galindo Km 30.5 Vía Perimetral, P.O. Box 09-01-5863, Guayaquil, Ecuador

7 School of Mathematics, University of Minnesota, Minneapolis, MN 55455, USA

MERRA-2	Modern-Era Retrospective analysis for research and application, version 2
MODIS	Moderate Resolution Imaging Spectroradiometer
OMI	Ozone Monitoring Instrument
PDC	Pyroclastyc Density Currents
$PM_{2.5}$	Aerodynamic particulate Matter < 2.5 µm
READY	Real-time Environment Applications and Display sYstems
SEM-EDX	Scanning electron microscopy coupled with energy disperse spectrometer
SENTINEL-5P	SENTINEL-5 Precursor
SO_2 mass density from MERRA-2	Sulfur dioxide column mass density [kg/m^2]
SO_2 total column density from TROPOMI	sulfur dioxide total column density [mmol/m^2]
TROPOMI	TROPOspheric Monitoring Instrument
UTC	Universal Time Conversion

Introduction

Volcanic eruptions are short to long-lasting events that are a source of ash particles and aerosols, which are released into the atmosphere over time. A significant portion of expelled volcanic ash can be carried by winds hundreds of kilometers away (Lettino et al. 2012; Woodhouse et al. 2013). Under proper meteorological conditions, energetic volcanic eruptions may even traverse the world—as is the case of the Pinatubo eruption in 1991 (McCormick et al. 1995) and the more recent Tonga volcanic eruption in Fiji (Zuo et al. 2022). Moreover, volcanic eruptions can act as a source of biogenic nutrients to inland fields (Langmann 2013) and oceanic environments (Hamilton et al. 2022), with an impact that can be measured on a local and global scale.

Distribution of the grain-size volcanic ash that falls depends on the degree of explosivity of the eruption, and the distance between the volcano and the plume axis (Bonadonna and Houghton 2005). Furthermore, from the chemical perspective, carbon dioxide (CO_2) and sulfur dioxide (SO_2) are typically among the chemical species released (Andreae 2007). When sulfur dioxide enters the atmosphere, it is oxidized and converted to gaseous sulfur acid, and these sulfate aerosol particles can be transported longer distances (Seinfeld and Pandis 1998). The sulfate aerosol is often used as a tracer for volcanic emissions. For instance, some researchers tracked a volcanic ash plume originating from the eruption of the Tungurahua volcano located in the Andes by the detection of SO_2 (Carn et al. 2011; Warnach et al. 2019), and recent studies utilize higher concentrations of SO_2 as an indicator for tracking volcanic emission trajectories (Makowski Giannoni et al. 2014; Saturno et al. 2018).

It has been reported that ash particles with sizes between 10 and 15 µm may produce throat irritation; smaller particles (less than 10 µm in diameter) cause asthma and bronchitis (Pohlker et al. 2021); and finer particles that have diameters less than 2.5 µm ($PM_{2.5}$) can cause serious respiratory diseases (Beckett 2000; Lelieveld et al. 2015). Overall, fresh erupted volcanic ash can produce detrimental consequences to human health such as irritation of the skin and eyes, while also increasing the risk of respiratory diseases such as asthma, and bronchitis in children (Forbes et al. 2003).

Ecuador, despite being a small country, contains approximately 85 quaternary volcanoes—a quarter of those volcanoes are still active and have been studied by many authors (Carn et al. 2008; Carn et al. 2011; Parra et al. 2016; Warnach et al. 2019). During the last 20 years, Cotopaxi, Tungurahua, and Reventador were among the most active volcanoes in Ecuador, and they are located within an area of approximately 200 km in diameter (Carn et al. 2011; Le Pennec et al. 2012; Gaunt et al. 2016; Parra et al. 2016). More recently, the Sangay, which is an active volcano located in the southwest part of Ecuador, has been a topic of attention due to its dynamic activity (Valverde et al. 2021; Bernard et al. 2022; Vasconez et al. 2022). On the days of June 9th, 2020; September 20th, 2020; and April 12th, 2021, a combination of more energetic eruptions from Sangay volcano and adequate meteorological conditions caused Guayaquil (a city with a population of 3 million located in the south-west sector of Ecuador) to be coated by a fine layer of volcanic ash of approximately 1 mm thick among all the events.

Volcanic eruptions are a recurrent phenomenon in Ecuador. There are many studies regarding macro particles (100 to 200 mm), but there is a lack of knowledge regarding natural airborne compounds generated from volcanoes and released into the atmosphere. Those particles are important for climate regulation (Zuo et al. 2022) and higher concentrations can produce detrimental effects on any living organism in its pathway (Stewart et al. 2021). Thus, the present study aims to (a) provide a detailed characterization of aerodynamic particle matter below 2.5 µm ($PM_{2.5}$) and meteorological parameters during Sangay's three volcanic eruptions between 2020 and 2021; (b) to analyze the long-range transport of Sangay plumes to the city; and (c) to provide a characterization of the particle structure, morphology, and chemical composition forming the volcanic ash that fell onto Guayaquil during the three volcanic emissions between 2020 and 2021. SEM and Energy Dispersive X-ray (point

EDX and mapping) were conducted on selected samples to study their physical properties and to identify and quantify their elemental compositions.

Methodology

The measurement of $PM_{2.5}$ suspended particles in the air during volcanic eruptions of the Sangay was carried out by using an air quality monitoring capability of measuring $PM_{2.5}$ in conjunction with the meteorological Weather Station WS-2000 from Ambient Weather (Ambient Weather Network) in the city of Guayaquil (−2.1588, −79.983 at 10 m asl). The Sangay volcano is in the Morona Santiago province which is part of the Ecuadorean Amazon region with geolocation (−2.005471, −78.340152 at 5282 m asl) and it is 175 km away east from Guayaquil. The time series of the meteorological data corresponds to the period from March 2020 to April 2021, when the eruption occurred. Variables such as precipitation, solar radiation, relative humidity, temperature, wind speed, and wind direction were collected, as suggested by Foken et al. (2021). The air quality data ($PM_{2.5}$) was collected using a Dylos DC-1100 (Dylos corporation) with a PC interface. A comparison of the Dylos DC-1100 and Meteo BAM 1020 was conducted. The comparison consisted of two different analyses: one conducted during the dry season (2018-12-02 to 2018-12-03) and one during the wet season (2019-02-06 to 2019-02-07). Results showed different correlation coefficients and estimates during the wet season ($r^2 = 0.85$; slope = 1.1, refer Fig. S1(a)) and the dry season ($r^2 = 0.82$, slope = 1.0, refer Fig. S1(b)) which is within the expected range of variability between measurements performed by these two sensors. Meteo BAM 1020 was located at −2.185990, −79.993165 at 5 m asl from our sampling point, which could also affect the comparison between the two sensors. The Meteo BAM 1020 was out of order in April 2019; consequently, the dataset from Dylos DC-1100 was the only device to measure $PM_{2.5}$ during volcanic emissions. Though these sensors present higher uncertainty (~15% in our case), a low-cost air sensor may be the solution for tracking pollution in emerging economy countries (Oyola et al. 2022) where other data sources are absent. The dates of interest, during which volcanic ash plumes were reported in Guayaquil, are (a) June 9th, 2020; (b) September 20th, 2020; and (c) April 13th, 2021.

Air mass characterization at the sampling point was conducted using the Hybrid Single-Particle Lagrangian Integrated Trajectory (HYSPLIT, NOOA-ARL, version 5.2) with meteorological input data from the Global Data Assimilation System (GDAS 1, 1° resolution) (Stein et al. 2015; Rolph et al. 2017; Draxler et al. 2018). The data corresponded to the period from January 1st, 2020, to December 31st, 2021, with 7 days of backward trajectories. Backward trajectories of Sangay volcano were analyzed at two heights: (a) 5000 m asl (to better visualize the volcanic plume trajectory path and to be aware of any physical obstacle such as the Andes mountain obstacles as suggested by Engwell and Eychenne (2016)) and (b) 1000 m asl (to visualize nearby potential sources as reported by Moran-Zuloaga et al. (2021)). Data was collected using HYSPLIT READY at the following site (https://ready.arl.noaa.gov/hypub-bin/trajtype.pl?runtype=archive, last visited on April 15, 2022). Once the backward trajectories were plotted, k-means clusters were used, and four clusters were selected as it is the categorization that best represents the main source paths using the minimum number of clusters. More details of the methodology for k-clustering and the elbow method selection can be found in the literature (Carslaw and Beevers 2013; Kassambara 2017; Pöhlker et al. 2019). The following satellite products were used: aerosol optical depth at 550 nm (AOD_{550nm}) at a wavelength of 550 nm from the moderate resolution imaging spectroradiometer satellite (MODIS) and the Aqua combined dark target deep blue AOD product with identification (MYD08_D3_v6) to visualize aerosol concentration from the regional perspective were implemented. The SO_2 column mass density [kg/m^2] level-2 (ENSEMBLE) was detected by using the Modern-Era Retrospective analysis for research and application, version 2 (MERRA-2, product identification M2T1NXAER v.5.12.4) satellite to visualize the path of the volcanic ash plumes. These products were obtained from NASA Giovanni (Geospatial Interactive Online Visualization and Analyze Infrastructure); see (Acker et al. 2014). The data was taken from the following website https://giovanni.gsfc.nasa.gov/giovanni/, last visited on March 30, 2022. SO_2 information from MERRA-2 satellite information was complemented with daily SO_2 total column density [$mmol/m^2$] information obtained from Copernicus Sentinel 5p using the TROPOspheric Monitoring Instrument (TROPOMI) (Fioletov et al. 2020). The vertical atmospheric profiles were analyzed from the Cloud-Aerosol Lidar and Infrared Pathfinder Satellite Observations (CALIPSO) (Winker et al. 2009) which has been demonstrated to be a useful tool to backtrack volcanic eruption plumes (Ritter and Münkel 2021). Lidar profiles from the Cloud-Aerosol Lidar with Orthogonal Polarization (CALIOP) datasets were consulted on: https://www-calipso.larc.nasa.gov/tools/data_avail/ last visited on April 16, 2022.

In addition to the automatic measurement of $PM_{2.5}$ and the meteorological variables, samples of the volcanic ash were collected during the different volcanic eruption events (Event 1: June 9, 2020, circa 02:00 UTC-5; Event 2: September 20, 2020, circa 12:00 to 16:00 UTC-5; Event 3: April 12, 2021, circa 09:30 UTC-5, as described in Fig. 1(g)). The samples were collected during the morning after each eruption between 08:00 and 08:30 am (UTC-5). To prevent contamination or remobilization of the ashes, masks and gloves were used and samples were handpicked and saved

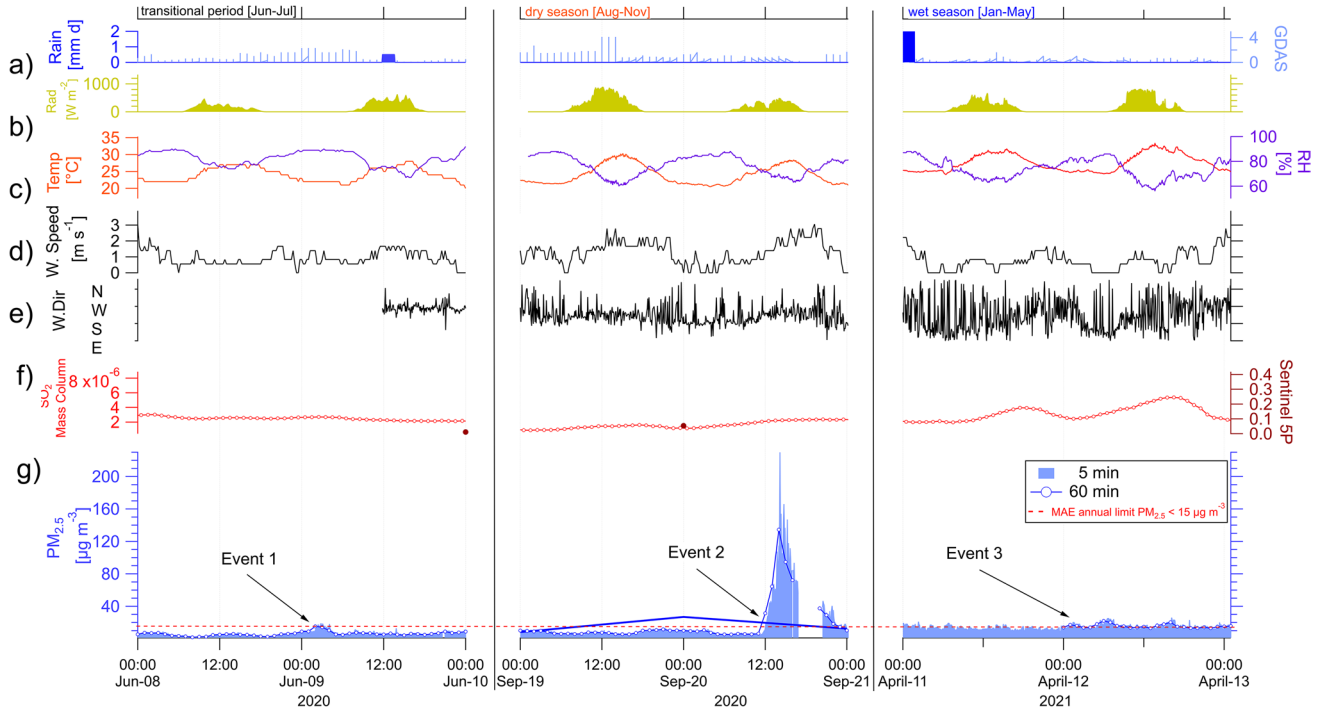

Fig. 1 Meteorological data of **a** rainfall in situ (left) and GDAS (right), **b** solar radiation, **c** temperature (left), relative humidity (right), **d** wind speed, **e** wind direction, **f** SO_2 from OMI [column density kg m^{-2}] (left) and from Sentinel 5P [column number density DU] (right), and **g** $PM_{2.5}$ in which shadows represent original resolution and lines and dots represent daily average data

into sample bags. All the samples were treated following the methodology of Horwell (2007). A laser scattering particle size analyzer (LA-300 Horiba) was used for grain-size distribution belonging to the Facultad de Ingenería en Ciencias de la Tierra (FICT), Escuela Superior Politécnica del Litoral de Guayaquil (Ecuador). More precisely, the analyzed macro particles were those between 62 and 0.5 µm in diameter. To avoid distortions of the measurements and ensure consistency of the data analysis, a 6 × 6 method was used: during data collection, each set of eruption samples (June 2020, September 2020, and April 2021) was measured 6 times and each sample was analyzed 6 times. The main statistical parameters (such as median, variance, standard deviation, skewness, and kurtosis) were determined according to Folk (1980) using the SFT software (version 2.19.0170)[1] to better characterize the fall deposits generally consisting of pyroclastic density currents (PDC) (Cioni et al. 2020).

Scanning electron microscopy (SEM) was applied to obtain insights into the structure, composition, and morphological characteristics of the ash samples collected. Precautions were taken during the sampling and storage of the ash to prevent moisture absorption as fresh volcanic ash can be hygroscopic (Gislason et al. 2011). The black and white SEM images were collected using the secondary electron scanning mode, and the color images show X-ray elemental maps from the same region as the SEM image. Energy dispersive X-ray spectroscopy EDX maps were conducted on the entire aggregate, and the results are presented through the colored map assemblies. Lower-resolution SEM imaging was employed to collect an overview of the ashes. SEM images were collected at the CIDNA laboratory in Ecuador by placing the ashes on an electrical conductive double-sided carbon tape fixed to the surface of an aluminum (Al) substrate, as shown in Fig. 5 and described in our previous work (Moran-Zuloaga et al. 2021). More advanced SEM studies were conducted at the University of Oklahoma by a modern SEM with EDX capabilities. The ash was dispersed on the surface of an aluminum disk using methanol, and double-sided electrically conductive carbon tape was not used—enabling the detection of elemental carbon in the samples. Before inserting the sample disk into the SEM chamber, the Al disk (with the sample on its surface) was exposed to the sputter coater (Emitech K-575D) for approximately 16 s. The sputter coater deposited a very thin layer (~4 nm) of iridium (Ir) on the surface of the sample. The SEM is a Thermo-Quattro S-field-emission environmental scanning electron microscope (FE-ESEM) from Thermo Fisher Scientific with elemental identification capabilities (spot and mapping). Based on this data, a PERMANOVA

[1] Source: https://www.lanl.gov/orgs/ees/geodynamics/Wohletz/KWare/Index.htm

analysis was performed to analyze potential statistical differences in chemical composition between the samples.

The backscattered electron (BSE) mode takes advantage of the elastic collisions between the electron beam and the atoms within the sample. Larger atoms scatter more electrons compared to smaller atoms, creating a higher signal (brighter spots on the SEM-BSE image). The number of backscattered electrons reaching the detector is proportional to the atomic number of the atom impacted by the electron beam. This phenomenon allows BSE to distinguish between different elemental materials, providing images that convey rudimentary information on the sample's composition (Mills and Rose 2010).

Data analysis was performed with R program (version R 4.2.0) (R Development Core Team 2021) coupled with the RStudio (open source program, version 2022.02.3) (RStudio Team 2020) and packages: openair (Carslaw and Ropkins 2012), maps, mapdata, mapproj, shapefile, rgdal, lubridate, dpltr, tidyr, maptools, reshape, and vegan. The igor pro (version 8.04) was used for further calculations and data analysis map script templates (Pöhlker et al. 2019) for data analysis and plotting. Temporal series of TROPOMI for SO_2 data was developed in Google Earth Engine (Gorelick et al. 2017).

Results

$PM_{2.5}$ concentrations and seasonality in 2020–2021

The meteorological conditions and $PM_{2.5}$ concentrations in Guayaquil were highly variable during the study period with three well-defined seasons: (1) the rainy period (Jan–May), (2) a dry period (Aug–Nov), and (3) a transitional period (Jun–Jul) occurring during the dry to wet seasons. Event 1 (June 9, 2020, during the transitional period from wet to dry season) is a period characterized by sporadic rain events—for instance, there was 0.5 mm of precipitation—with a mean temperature of 26 °C and an average relative humidity of 72%. During this event, the wind speed was low (average wind speed was 0.5 m s^{-1}) and mostly characterized by a southwest direction. During cloudy weather, an average solar radiation of 112 W m^{-2} was achieved (Fig. 1, left panel). During Event 2 (September 20, 2020), the average temperature was 24 °C and the average relative humidity was 77% with no rainfall. This is a cold windy period with an average wind speed of about 1 m s^{-1}, mostly in the southwest direction. This was a cloudy period with a mean solar radiation of about 108 W m^{-2} (Fig. 1, middle panel). Event 3 (April 12, 2021) occurred during the wet season (Jan–May) with an average temperature of 28 °C and average relative humidity of 73%. During this event, there was no precipitation, and the average wind speed was 1 m s^{-1}; wind direction varied from north, south, east, and west. The solar radiation was 181 W m^{-2} (Fig. 1, right panel).

The values of $PM_{2.5}$ during the wet season of 2020 were lower (6 ± 2 µg m^{-3}) than in the transitional season in 2020 with $PM_{2.5}$ of 8 ± 4 µg m^{-3}. In 2020, due to COVID-19 restrictions and fewer people traveling by combustion vehicles, the concentration of $PM_{2.5}$ dropped to 4 ± 3 µg m^{-3}. Nonetheless, once human activities returned to normal, the $PM_{2.5}$ concentrations increased to 16 ± 3 µg m^{-3} by the end of the year (Fig. S2(e)). It is important to note that this data was measured with a low-cost sensor Dylos DC-1100 located at −2.1588, −79.983 at 10 m asl. A comparison between this instrument and a Meteo BAM 1020 located at −2.185990, −79.993165 at 5 m asl showed good correlation values (Fig. S1). However, the measured Dylos DC-1100 values tended to overestimate $PM_{2.5}$, particularly during the wet season.

The Geophysical Institute of Escuela Politécnica Nacional of Ecuador (IG-EPN) provided three alerts of volcanic ash warnings with their in-house forecast service (reports: https://www.igepn.edu.ec/servicios/noticias, and Twitter account @IGEcuador). The three volcanic plumes of long-range transport pollution occurred during 2020 and 2021, specifically on (a) Event 1: June 9th, 2020, (b) Event 2: September 20th, 2020, and (c) Event 3: April 13th, 2021. Event 1 occurred during COVID-19 lockdown restrictions. On June 9th at 01:00 UTC-5, there was an alert regarding the Sangay volcanic plumes, and the ashes were deposited in Guayaquil later that morning.

The $PM_{2.5}$ concentrations measured on June 9th, 2020 using Dylos DC-1100 showed hourly average values of 15 ± 2 µg m^{-3} at 02:00 UTC-5 (considering June 2020 $PM_{2.5}$ avg. was 10 ± 5 µg m^{-3}). At this time, there was restricted human mobility due to COVID-19. During Event 2 (occurring on September 20th, 2020 at 04:00 UTC-5), the volcanic plume started at 12:00 and lasted until 16:00 UTC-5, producing an hourly average $PM_{2.5}$ values of 133 ± 40 µg m^{-3} (note that September 2020 $PM_{2.5}$ avg. was 13 ± 11 µg m^{-3}). At the time, COVID-19 restrictions were relaxed, and human mobility had returned to normal levels. Lastly, Event 3 occurred on April 12th, 2021, at 01:00 UTC-5, prompting another volcanic alert. Event 3 produced $PM_{2.5}$ hourly avg. 17 ± 2 µg m^{-3}, which lies within the range of urban background conditions (considering April 2021 $PM_{2.5}$ avg. 16 ± 3 µg m^{-3}). It is worth mentioning that in April, activities were back to normal. Therefore, it is assumed that those values correspond to urban background conditions (Fig. 1(h)).

Back trajectory analysis, cluster classification, and atmospheric vertical profiles

The 7-day backward trajectories (BT) during the study period at 1000 m asl helped identify in situ sources in the city of

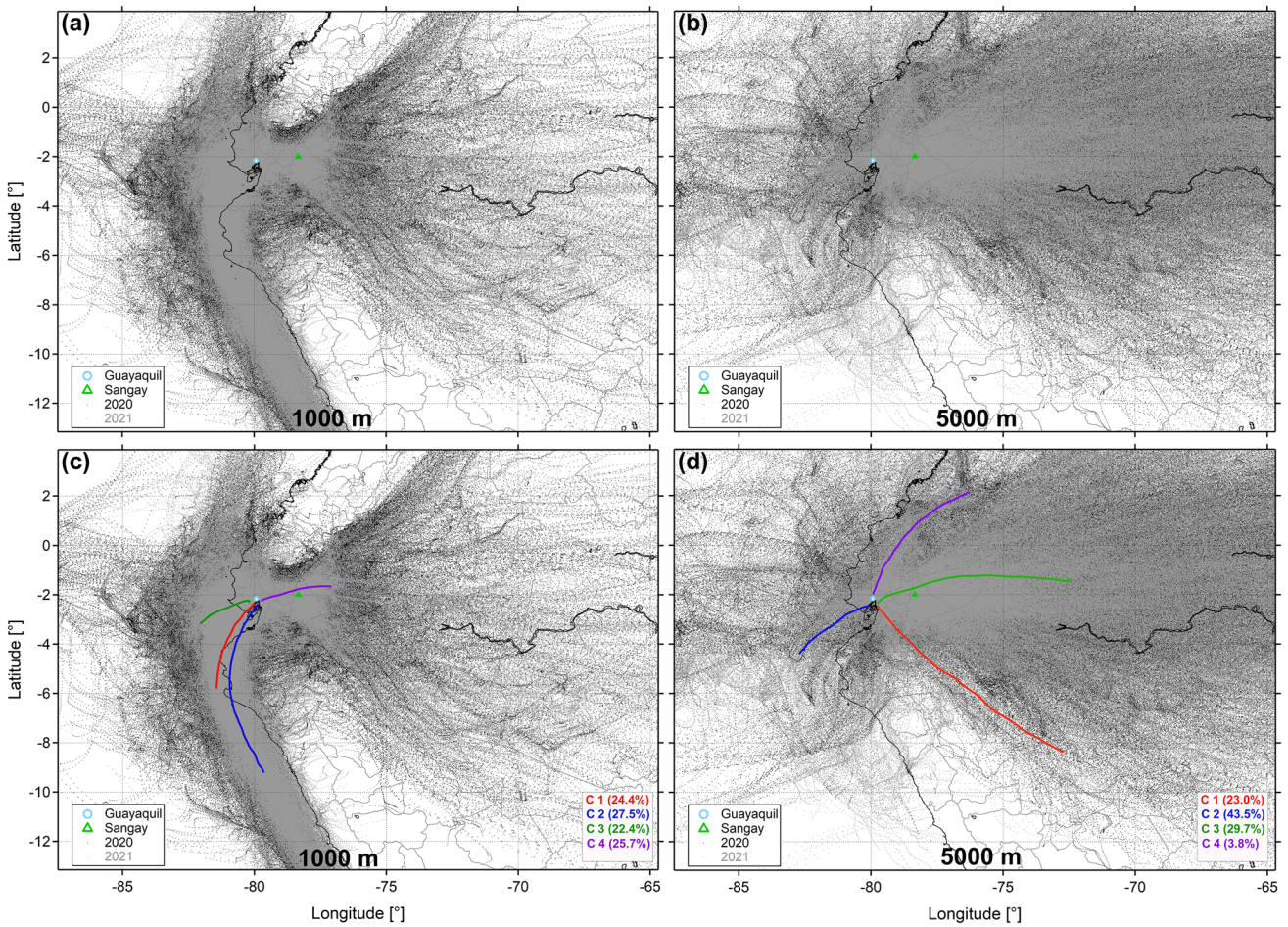

Fig. 2 Backward trajectories **a** at 1000 m and **b** at 5000 m and cluster classification of air masses at **c** 1000 m and **d** 5000 m during 2020 and 2021.

Guayaquil (Fig. 2a). Meanwhile, Fig. 2b represents the 7 days backward trajectories at 5000 m asl from 2020 and 2021, this BT shows the wind path and sources around the volcano. The 1000 BT shows a well-defined trend from the south, and southwest air masses (Fig. 2a), while the 5000 BT shows east-to-west air masses trends that help identify the path of the ash plumes generated by the Sangay volcano (Fig. 2b).

The results of BT at 1000 m indicate that there were four different clusters of air masses arriving in the city, which are referred to as C-1 to C-4. The C-1 (24.4%) represents mid-range southwest, the C-2 (27.5%) is a long-range path from south and southwest, the C-3 (22.4%) is a mid-range from the west, and the C-4 (25.7%) represents a mid-range path from the east. At this altitude (1000 m asl), there are strong wind events from the south and southwest that are well-defined (Fig. 2c). Backward trajectories at 5000 m were also grouped in four clusters. The C-1 (23%) portrays a long range from the south and south-east, the C-2 (43.5%) represents a long range from the west, the C-3 (29.7%) represents the mid-range from the east, and the C-4 (3.8%) describes the mid-range from the north (Fig. 2d). Despite the differences in the BT at the two heights (1000 and 5000 m), they showed a remarkable trend from the east and southwest directions. At higher altitudes, there was dominance from east to west and a minor degree of a southwest path.

Climatic conditions seemed to be a direct driver of the long-range transport occurring in the three volcanic eruptive events. Evaluating the individual backward trajectories shows Fig. 3a–d and Fig. 3b–e that during Event 1 and Event 2, there is an influx of air masses from the north and east, such occurrences are not present during Event 3 for 1000 or 5000 m asl; this corresponds to the volcano's height (Fig. 3c–f). At 1000 m asl, there is a similar trend between the transitional and the dry seasons in contrast with the wet season (Fig. 3a–c). At 5000 m asl, the east trend path is present during all three events, along with some broader trends towards the northeast during the wet season (Fig. 3d–f and Fig. S1). This seasonality effect, from the transitional period towards the dry season with the strong presence of winds, may explain the transport of volcanic plumes that occurred during volcanic Events 1

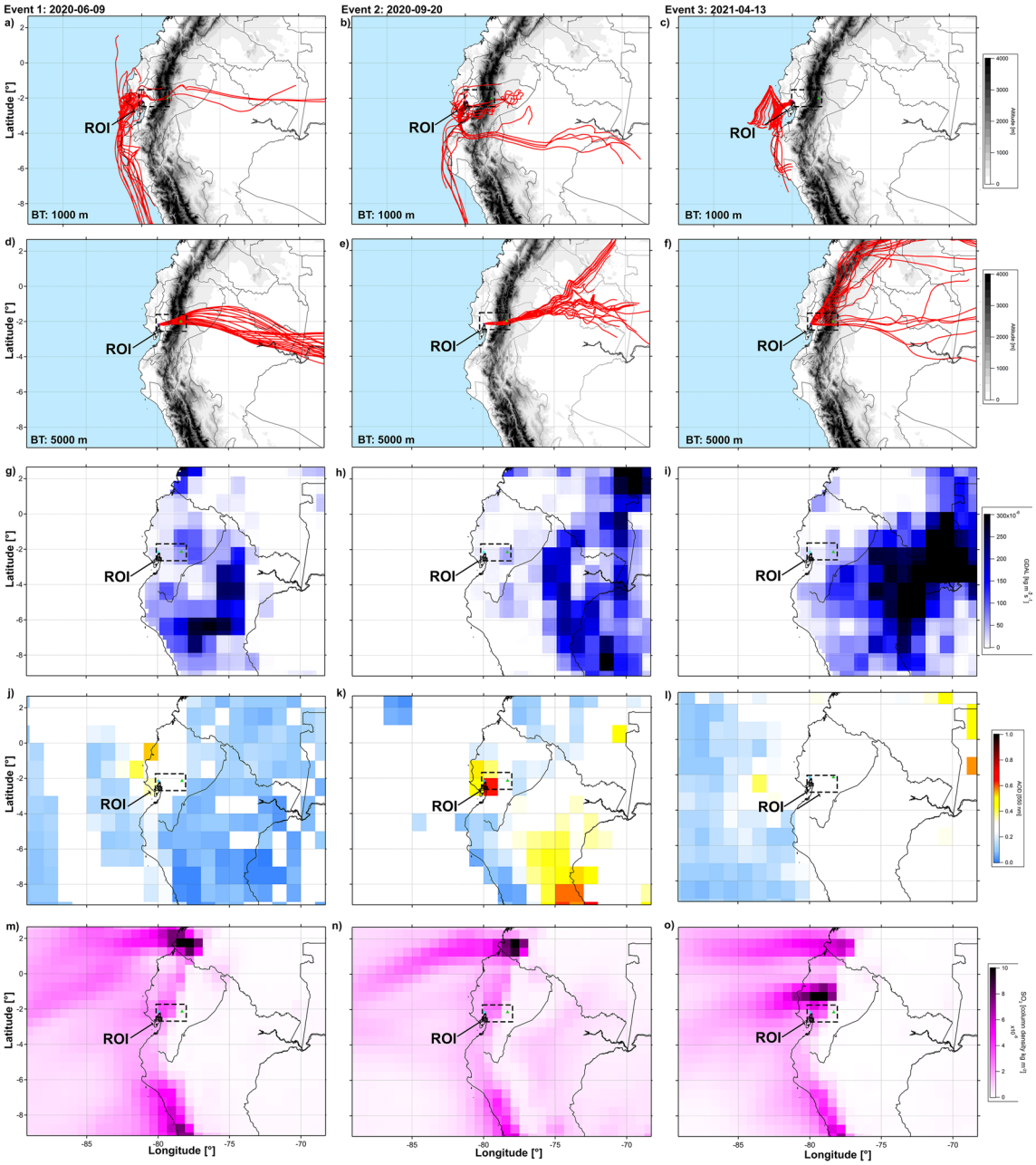

Fig. 3 Satellite products BT (1000 m, 5000 m), GDAS [kg $m^{-2}s^{-1}$], AOD [550 nm], SO_2 [column density kg m^{-2}] from **a** June 9, 2020, **b** September 20, 2020, **c** April 13, 2021. Rectangular shape represents the Region of Interest (ROI) from the Guayaquil and Sangay volcano

and 2. In parallel, the precipitation rate is almost absent during the transitional (Fig. 3g) and dry seasons (Fig. 3h), but it is stronger during the wet season (Fig. 3i).

This is also reflected in the AOD 550 nm maps, which help to identify a possible niche of aerosol concentrations. As observed in Fig. 3j, k, AOD is higher during the transitional and the dry seasons than during the wet season—this corresponds to when most particles were scavenged before reaching the city in the form of wet deposition (Fig. 3l). Thus, higher aerosol values (0.4 correspondence of aerosol levels) could be observed during the absence of rain while AOD during the wet season is very low. SO_2 total mass column was higher during the transitional and dry seasons (Fig. 3m, n), and significantly lower during the wet season (Fig. 3o). SO_2 results were very similar to those found on AOD (Fig. 3j–l).

The vertical profiles from 0.2 to 20 km using CALIPSO during the volcanic emission plumes are visible in Fig. 4. As observed on June 8, 2020, at 07:07:46.8 UTC (Event 1), there were certain traces of some polluted dust at 10 km asl, with other traces—such as smoke, polluted

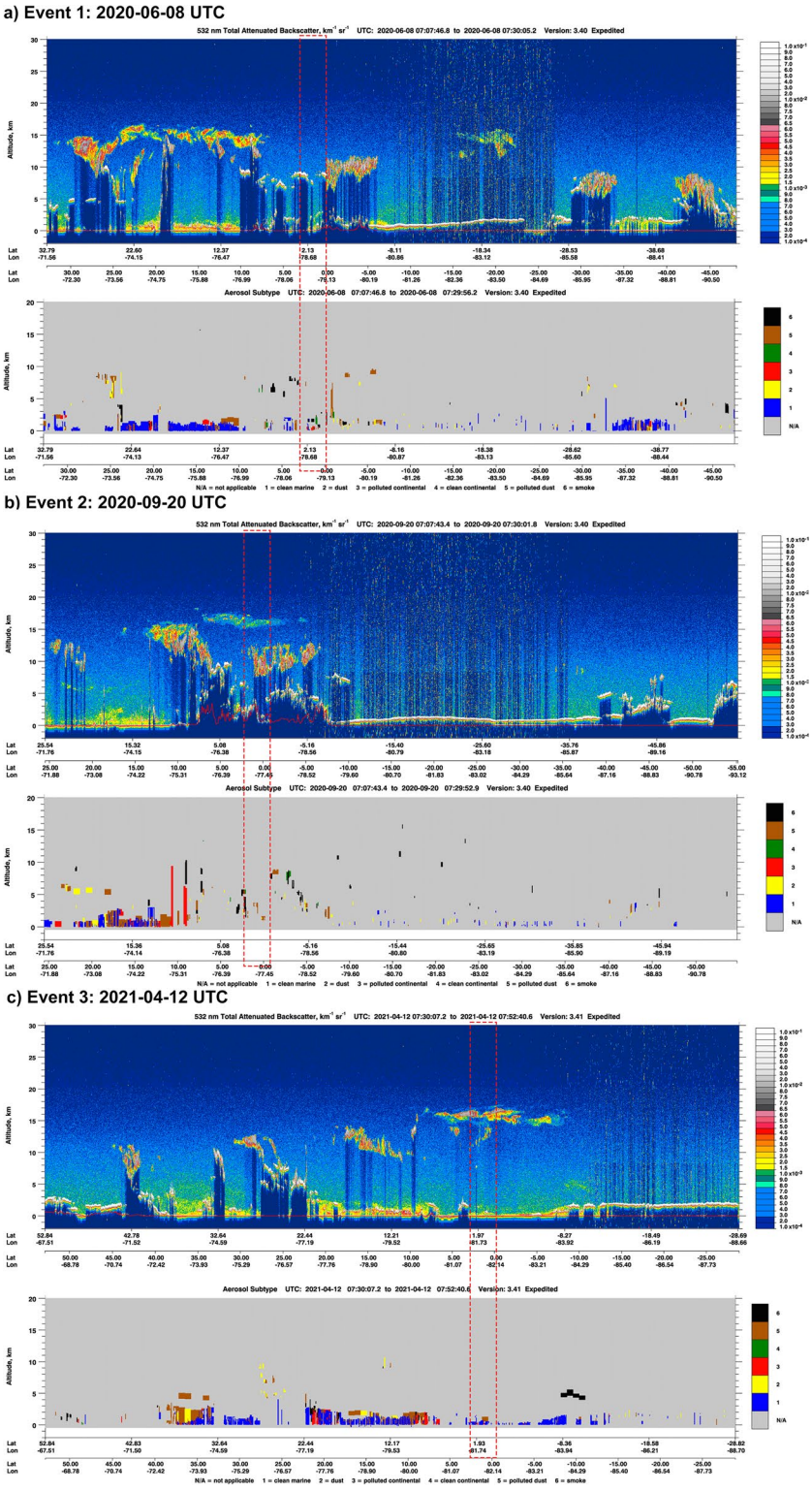

Fig. 4 Vertical profiles from CALIPSO: **a** June 8, 2020, **b** September 20, 2020, and **c** April 12, 2021

Table 1 Main statistical parameters of macro particle volcanic ash samples fell in Guayaquil in June and September 2020 and April 2021.

Sample	Median	Variance	Standard Deviation	Sorting	Skewness (Sk)		Kurtosis (K)	
	μm	μm^2	μm		μm		μm	
June 2020	55.8	2417.4	49.1	Poorly sorted	−0.383	Very fine skewed	1.293	Leptokurtic
September 2020	35.2	1237.9	35.2	Poorly sorted	−0.382	Very fine skewed	1.102	Mesokurtic
April 2021	41.1	1094.4	33.1	Poorly sorted	−0.359	Very fine skewed	1.439	Leptokurtic

continental, and clean continental air—suspended at 5 km asl (Fig. 4a). On September 20, at 07:07:43.4 UTC (Event 2), there were traces of smoke and polluted dust suspended in the air at 10 km asl; below 2 km asl, there were some traces of clean marine air (Fig. 4b). Finally, Event 3, on April 12, 2021, at 07:52:40.6 UTC, presented a clean marine breeze at 2 km asl (Fig. 4c). Event 2 was the most dust polluted, with ash clouds displaced from east to west.

Physical features of Sangay distal volcanic ash

The grain size analysis was conducted across a range of different magnifications on a sample composed of more than 200 particles—this number of particles was used to ensure that the measurements are statistically representative (Lettino et al. 2012). Volcanic ash macro particles can exhibit different features due to the type of eruption, fragmentation, and transport process as mentioned by Mulas et al. (2019). The June 2020 sample had a unimodal trend, and it has a median particle diameter of 55.8 μm. It is poorly sorted, which indicates that there is a large variability in the macro particle size distribution of ashes particles (there is a large variance within sizing), whereas well sorted indicates that the deposit ashes have a more uniform size (there is a low variance). The particle samples tended to be very fine-skewed and leptokurtic. The September 2020 sample had a bimodal trend with a median particle diameter of 35.2 μm. It is poorly sorted, very fine skewed, and mesokurtic. The last volcanic ashes fallout in Guayaquil in April 2021, had a unimodal trend with a median particle diameter of 41.1 μm. It is poorly sorted, very fine skewed, and leptokurtic (Table 1).

According to IGEcuador reports[2], the volcanic column height in September 2020 (Event 2) and April 2021 (Event 3) reached altitudes up to 7 km above the vent, while in June 2020 (Event 1), the volcanic column height reached altitudes of 3 km above the vent. The higher the column, the stronger the volcanic explosion; therefore, Event 2 and Event 3 were stronger than Event 1. The grain size analysis of the ashes deposited in the city has a double hump shape, one hump at a median of 3 to 4 μm of particle diameter (above $PM_{2.5}$), and a second at a median of 60 to 70 μm (macro particles). From the $PM_{2.5}$ perspective, these results confirmed that Event 2 and Event 3 were more energetic than Event 1. Consequently, Event 2 produced more ash pollution than Event 3, and finally Event 1, according to the ground measurements. Hence, $PM_{2.5}$ from Event 2 may have produced out-scale airborne particles, which could be caused by the Dylos DC-1100 sensor being overloaded by very large particle concentrations during a short period. In parallel, larger median particle diameters between 35 and 56 μm in diameter size (granulometry analysis) presented a different scenario. Hence, in Event 3, there were deposited larger particles than in Event 1 and Event 2 (Fig. S3). According to this finding, the distance traveled by the deposited volcanic ash is closely related to the force of each eruption and linked to the meteorological conditions (e.g., precipitation, wind speed, wind direction) and its predisposition to facilitate long-range transport, and, as shown in Fig. S5, forward trajectories tend to favor the long-range transport of Sangay ashes.

Microscopy analysis of volcanic ashes

Figure 5a represents a lower-resolution SEM image of the volcanic ash in which the size variation of the particles or fragments in the ash is visible. As shown in Fig. 5a, fragments are composed of very large size grains and very fine materials.

Large size fragments (particle matter > 10 μm) The high-resolution SEM images Fig. 5b–g, allow for a close-up view of the external morphology of the large fragments. There is a significant variation in the external morphology of the fragments ranging from smooth, spherical-like shapes to irregular shapes with sharp edges (Fig. 5b). The HR-SEM images reveal the presence of unique fixtures on the fragments' surfaces that resemble what is known in the literature as a "vesicle imprint," with almost perfect diameters as indicated by the solid arrows in Fig. 5b, d, f, g. A similar external morphology can be seen in the fragment shown in Fig. 5b. However, this type of morphology is referred to in the literature as "spongy." The surface of the "spongy" fragment is rough, curved, and irregularly shaped as a result of

[2] Source: https://www.igepn.edu.ec/servicios/busqueda-informes

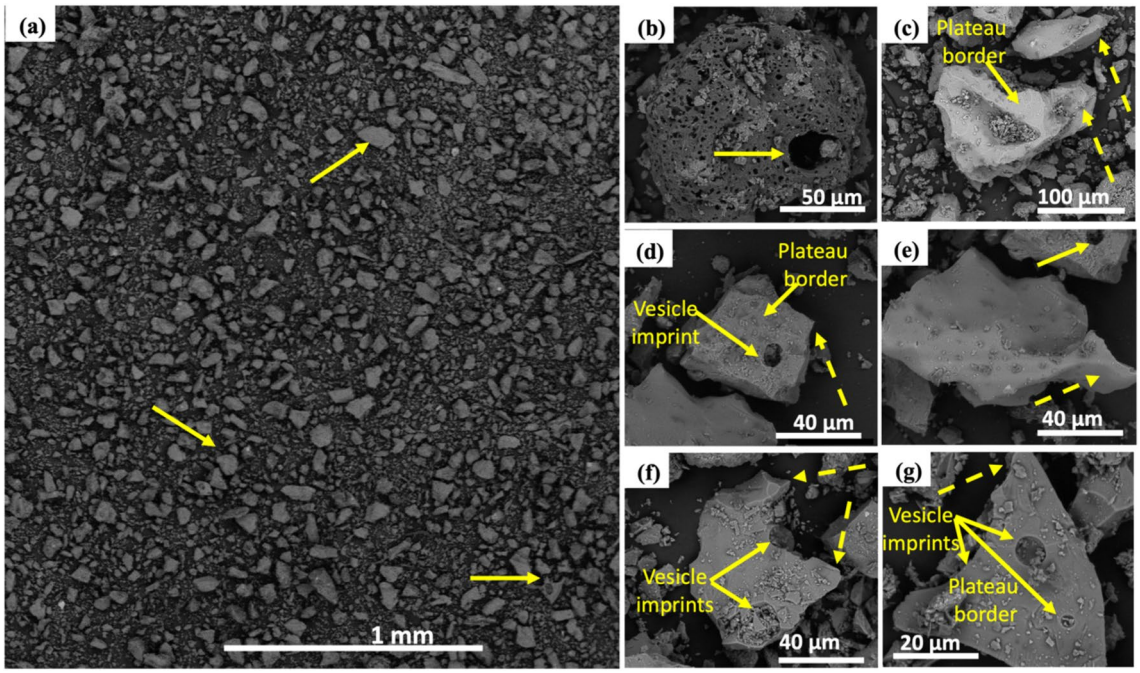

Fig. 5 SEM images of volcanic ashes with a wide range of sizes and morphology of the long-range transport erupted by the Sangay and collected in Guayaquil. June 9, 2020 (**b**, **c**), September 20, 2020 (**d**, **e**), and April 13, 2021 (**f**, **g**).

the rupture of randomly oriented spherical to elliptical vesicles (Genareau et al. 2013; Liu et al. 2015; Liu et al. 2016; Wilcox et al. 2019). The fragment in Fig. 5e has an elongated morphology and its surface appears to be smooth. This type of structure is known in the literature as "fluidal." It has been stated that an elongated shape is due to the result of interconnected tubular vesicles (Pompilio et al. 2017). The fragment shown in Fig. 5d is "blocky" and displays multiple fracture-bounded surfaces alongside some smoother facets.

Another unique fixture of the Sangay ashes is that some fragments have multiple vesicle imprints on a single facet (Fig. 5g); some of these vesicle imprints are filled with a finer-grained material, consistent in all SEM images. The sharp-edged fixture of some of the ash fragments remained sharp despite its long jet trajectory from Sangay to Guayaquil; the dotted arrows in Fig. 5c–g correspond to a sharp edge on the pictured fragments. Furthermore, the large grains appear to be decorated by smaller and finer materials/particulates on their surfaces, as can be seen in the HR-SEM images (Fig. 5). This effect could be caused by volatile gases condensing on the surface of the ash particle as that particle is vented from the volcano's crater—forming these finer materials.

Fine size fragments (particle matter < 2 µm) Electron microscopy was also employed to characterize the morphology of the volcanic fine-grain fragments (< 2 µm) that frequently accompany the larger fragments (i.e., up to 0.25 mm). It is observed that for all three volcanic eruptions, the external morphology of the finer structures is different from that of the larger fragments. The finer particles do not have sharp edges, and their surfaces do not display the typical "spongy" morphology nor any "vesicle imprints" (Fig. 6). For all three cases, point EDX and EDX-elemental mapping were applied. Figure 6a is the microstructure of the analyzed aggregate collected from the eruption on June 2020 and used for point EDX of selected individual fragments and for obtaining the EDX maps of the entire area. The SEM images (black and white contrast) are from secondary electron mode while the color images are from X-ray elemental maps of the same region shown in the SEM image. The SEM secondary electron image (Fig. 6a) shows that particles in the aggregate have a polydisperse size distribution. The larger particle in this aggregate is about 4 µm in size surrounded by finer particles (< 2.5 µm). The point EDX spectrum of selected particles forming the aggregate is displayed in Fig. 6(a1–a5). EDX maps were conducted on the entire aggregate and the results are presented through the colored map assemblies (Fig. 6(b1–b8)). The table (Fig. 6b) represents the EDX component analysis of the fragments in % wt. and % at. using the EDX maps of elements, including C-K, O-K, Na-K, Mg-K, Si-K, S-K, and Fe-K; the values are based on the entire aggregate/cluster shown in the SEM image captured in Fig. 6a. It should be noted that electrically conductive carbon tape was not used to secure the structures to the Al substrate for SEM studies; therefore, all

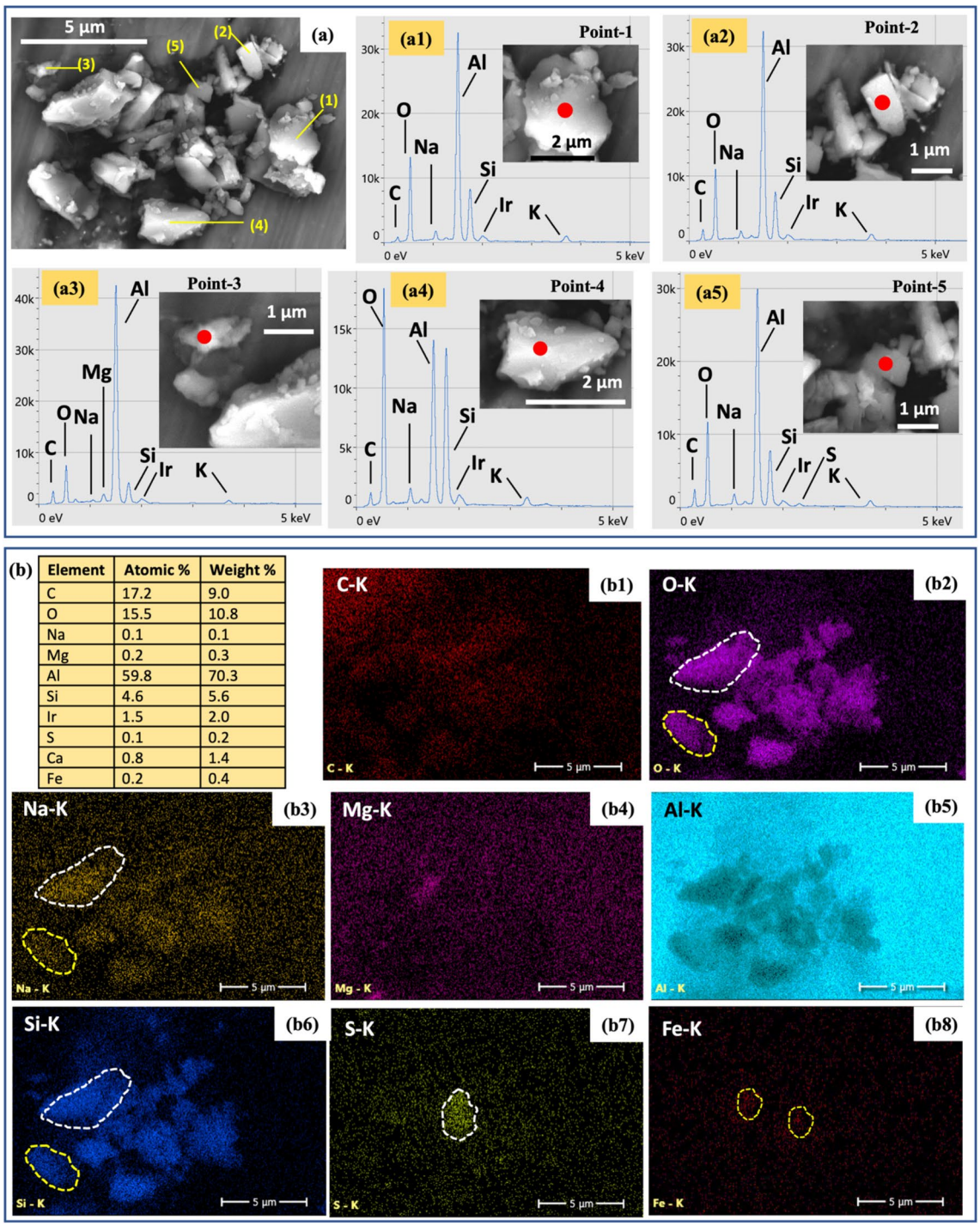

Element	Atomic %	Weight %
C	17.2	9.0
O	15.5	10.8
Na	0.1	0.1
Mg	0.2	0.3
Al	59.8	70.3
Si	4.6	5.6
Ir	1.5	2.0
S	0.1	0.2
Ca	0.8	1.4
Fe	0.2	0.4

Fig. 6 (a1–a5) Energy dispersive X-ray spectroscopy (EDX) spectra of the Sangay volcanic samples collected on June 2020 along EDX maps of C-K, O-K, Na-K, Mg-K, Al-L, Si-K, S-K, and Fe-K (b1–b8). The microstructure of the analyzed aggregate is shown in the secondary electron SEM image (**6a**). The Al signal is partially attributed to the nature of the SEM analysis where an Al substrate is used to hold the sample under the electron beam. The Ir is contributed from the sputter coating. Please be aware that from (a1) to (a5), *y*-axis scales are different in scale to emphasize each element's peak.

carbon measurements should originate from the ash samples. Hence, it seems that fine-grain materials consist of a certain percentage of carbon. Through the EDX maps, it is observed that the structures appear to be rather chemically well mixed in the context of the major chemical species forming the samples. For instance, by comparing the

EDX maps of Fig. 6(b2) with Fig. 6(b6), the shapes of the fragments resemble each other, despite one map representing oxygen (light purple) and the other silicon (light blue). Additionally, sulfur (green) and iron (red) appear to be more localized as shown by the circled areas forming particles (Fig. 6(b7,b8)). It is evident from the SEM images that the selected samples are composed of particles smaller than 1 µm (Fig. 6(a5)). EDX elemental mapping of the aggregates over the entire region in Fig. 6a resulted in 59.8% at. and by 70.3% wt. for Al. The high Al reading originates from the Al substrate on which the sample is placed. The SEM analyses were repeated with a special carbon substrate and revealed that the elemental composition of Al is typically less than 2%, and this was the case for all samples of the various studied eruptions.

The secondary electron SEM image in Fig. 7c is from a selected sample of ashes from the volcanic eruption collected in September 2020. The point EDX spectrum of selected fragments is displayed in Fig. 7(c1–c5). The color images in Fig. 7(d1–d8) represent EDX maps collected on the entire region of the SEM image in Fig. 7c. The SEM image in Fig. 7c indicates the area used for the EDX maps and the variety of microstructures present in the analyzed aggregate. Figure 7(d1–d8) reveals the relatively widespread distribution of elements including C-K, O-K, Na-K, Mg-K, -L, Si-K, S-K, and Fe-K. The ashes of June and September eruptions appear to be composed of relatively large particles accompanied by very fine particles in the order of a few microns in size (Fig. 7). The table in Fig. 7d represents the % at. and % wt. of key elements of the fragments shown in Fig. 7c. Similarly, the Al reading in the spectrum originates from the substrate used to hold the particles for the SEM study. The major chemical species of the sample are C (~7.4% at.), O (~14.2% at.), and Si (~4.8% at.). It can be observed that for this aggregate, the EDX Fe-Maps resulted in ~0.3% at. (Fig. 7(d8)). It is also evident that the carbon element present in this aggregate is much smaller compared to the previous aggregate. It can be observed that the carbon peak in the EDX spectra (Fig. 7(c1–c5)) is not the same. That is, some structures appear to have more carbon than others. For instance, the EDX mapping in Fig. 7(d1) (color image) correlates well with the point-EDX spectrum in Fig. 7(c5). Similarly, there are relatively stronger peaks on particle point-3.

EDX maps and points from the April 2021 event (Fig. 8) are similar to the volcanic ashes collected from the June and September 2020 eruptions, the major chemical species forming the fragments are C, O, and Si, with atomic percentage values of C (~11.1% at.), O (~13.9% at.), and Si (~3.0% at.). Like the previous eruptions, the EDX mapping shows that the structures of the samples collected in April 2021 appear to have their principal elements chemically well mixed. That is, the X-ray elemental maps of the fragments appear well-defined in several of the color images, and they correlate well with the structures present in the secondary electron SEM image (Fig. 8(e)). For instance, the same well-defined particle is evident for O (purple, Fig. 8(f2)), Na (yellow, Fig. 8(f3)), and S (green, Fig. 8(f7)). Similarly, the C (Fig. 8(f1)), O (Fig. 8(f2)), and Si (Fig. 8(f6)) present in the structures have very similar appearances. It is also evident in the X-ray elemental maps that the shape of a few particles displays strong signatures of Na (Fig. 8(f3)), S (Fig. 8(f7)), and Fe (Fig. 8(f8)). A simple inspection of the point EDX spectra Fig. 8(e1–e5) shows that the C peak is relatively stronger than in previous cases. A performed PERMANOVA analysis was conducted to analyze any potential statistical difference in the overall composition of the samples between ash events (differences in the weight of the different components). Different points within each picture were treated as replicates and the picture ID, representing each ash event, was a fixed factor in the analysis. The PERMANOVA analysis showed no differences between images in the composition of the different points ($Pr > F = 0.912$), refer to Table S2. It is important to remark that the presented analysis corresponds to a small portion of selected samples; further exploratory analysis may be needed for corroborating the results.

Discussion

The city of Guayaquil receives clean air breezes during the wet season and the city is vulnerable to external sources of pollution (biomass burning, volcanic ashes, etc.) during the dry season when winds can be an active transporter of dry deposition pollutants (Moran-Zuloaga et al. 2021). During the wet and transitional seasons (Jan–Jul), there were frequent precipitation events and high humidity values as mentioned by Cañadas Cruz (1983). Consequently, during Event 1 (transitional period; Fig. 3a–g) and Event 3 (wet period; Fig. 3c–l), most volcanic plume dispersions are modulated by meteorological conditions. In contrast, volcanic plumes are more prone to travel long distances during the dry season (Event 2; Fig. 3b–h), when specific climatic conditions such as high wind speeds from the continental topography to the coast occurred. Ecuador is a country with many volcanic eruptions (Wilson et al. 2012). The mobility restrictions due to COVID-19 pandemic events represent a significant reduction of the well-known anthropogenic pollution (Crutzen 2021) and allow us to observe the volcanic plume ashes $PM_{2.5}$ contribution within its whole magnitude.

Under normal conditions, the wet season usually is a cleaner period because of wet precipitation occurring due to external pollutants. In contrast, the dry and transitional

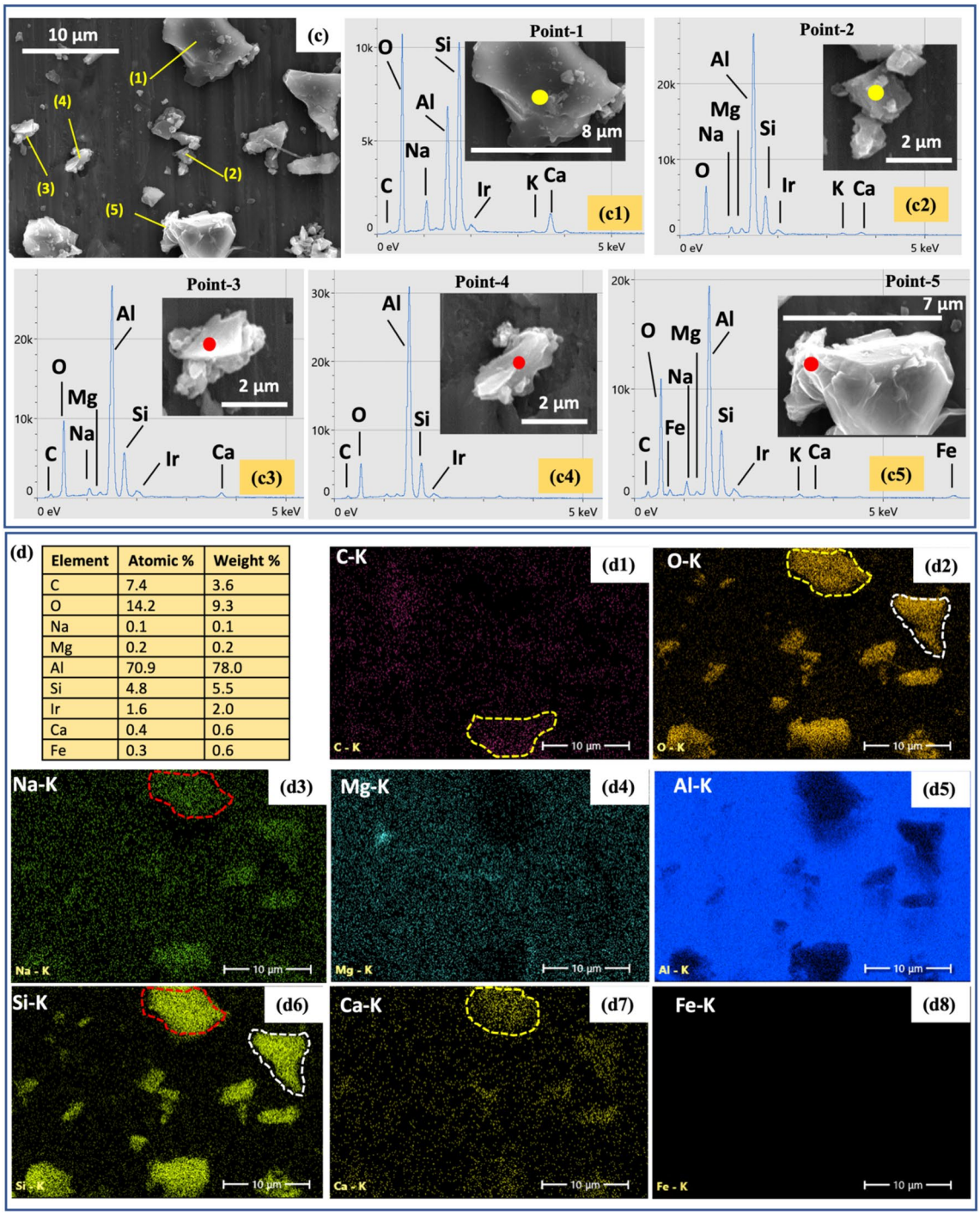

Fig. 7 (c1-c5) Energy dispersive X-ray spectroscopy (EDX) spectra of the Sangay volcanic samples collected on September 2020 along with maps of C-K, O-K, Na-K, Mg-K, Al-L, Si-K, S-K, and Fe-K (d1-d8). The microstructure of the analyzed aggregate is shown in the secondary electron SEM image (7c). The Al signal is partially attributed to the nature of the SEM analysis where an Al substrate is used to hold the sample under the electron beam. The Ir is contributed from the sputter coating. Please be aware that from c-1 to c-5 y-axis scales are different in scale to emphasize each element's peak

seasons are exposed to external pollutants due to high wind speeds and directions. During the present study, three different events occurred in the transitional, dry, and wet seasons. The wet season tended to be a cleaner period because of the recurrent wet precipitation, but during Event 3, the rain was absent during a spontaneous volcanic eruption, in which specific meteorological conditions favored the volcanic plume to reach the city of

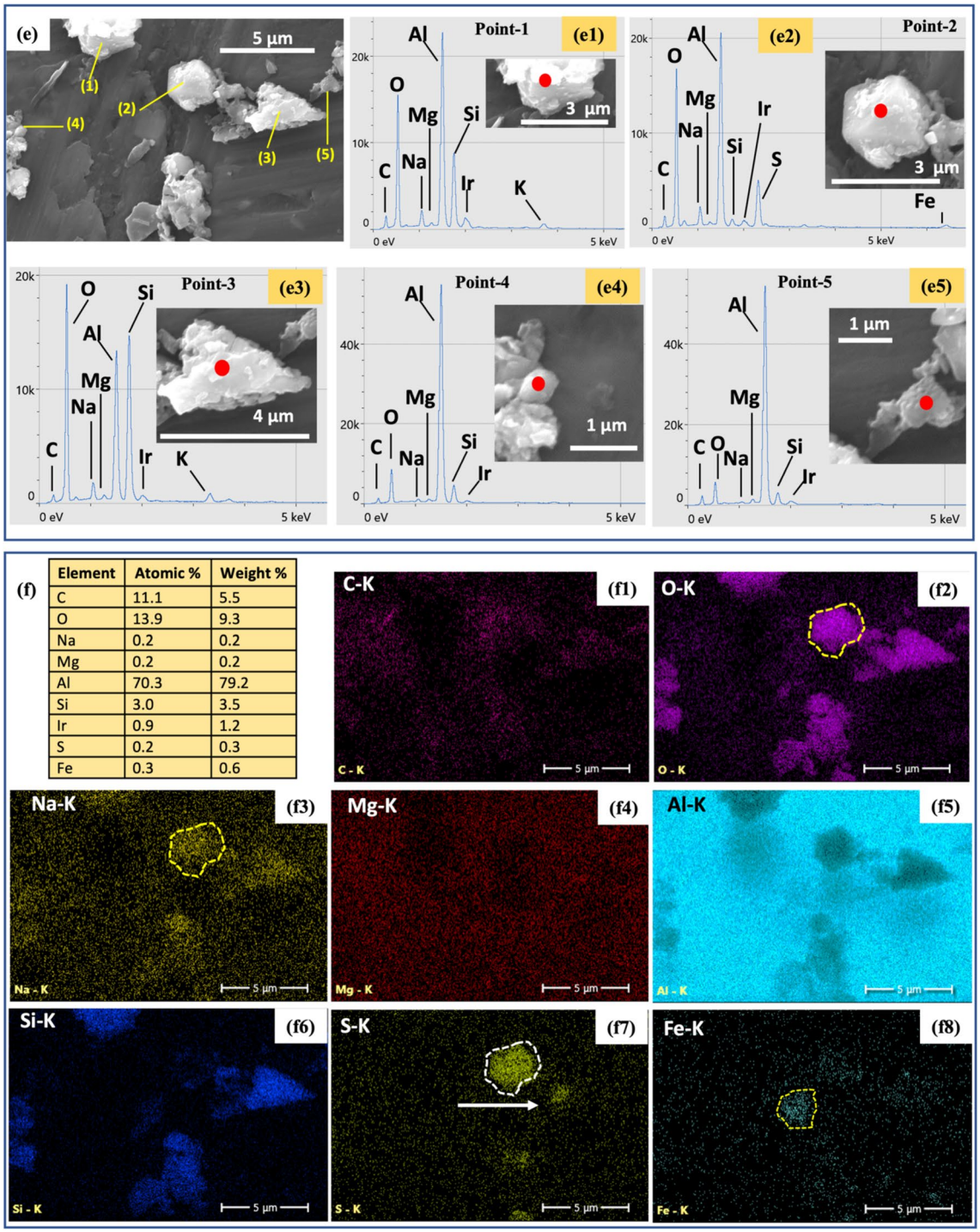

Fig. 8 (e1–e5) Energy dispersive X-ray spectroscopy (EDX) spectra of the Sangay volcanic sampled ashes collected on April 2021 along with EDX maps of C-K, O-K, Na-K, Mg-K, Al-L, Si-K, S-K, and Fe-K (f1–f8). The microstructure of the analyzed aggregate is shown in the secondary electron SEM image (8e). The Al signal is partially attributed to the nature of the SEM analysis where an Al substrate is used to hold the sample under the electron beam. The Ir is contributed from the sputter coating. Please be aware that from (e1) to (e5) *y*-axis scales are different in scale to emphasize each element's peak.

Guayaquil. Hence, previous studies on volcanic emissions in the Andes mountains exposed the vulnerability of all populations located to the west and southwest of Ecuador (Carn et al. 2011; Le Pennec et al. 2012; Parra et al. 2016; Bernard et al. 2022; Tadini et al. 2022; Vasconez et al. 2022), refer to Table S1.

Seasonality is a key element in the success of long-transport pollutants (Wu et al. 2018). As shown in Figs. 2 and 3 and Fig. S2, the total mass column of SO_2 was able to travel such significant distances and be deposited on the western continent due to favorable conditions. The AOD is strong during the dry season (Event 2) and when there was high wind speed from east to west (Fig. 3k). In contrast, during the wet season (Event 3) and the transitional season (Event 1), rainfall plays a key role in minimizing the middle-range and long-range transport elements that occur during the dry season (Fig. 3g–i), and this correlates well with $PM_{2.5}$ during the three events. SENTINEL 5P SO_2 has proven to be a good plume indicator for Reventador and Sangay volcanoes according to Markus et al. (2023). However, it was not the case in our study, but this discrepancy could be caused by poor meteorological conditions (Fig. S2(c) and Fig. S5).

The Sangay volcanic alert on September 20 (Event 2) started at 4 am (UTC-5) and the ash plume reached the city at around 8:00 UTC-5, according to the results obtained from the analysis of GOES-16 satellite data by Bernard et al. (2022). $PM_{2.5}$ concentrations during Event 2 corroborate these results as there was an increase of those particles at around 12:00 UTC-5 lasting for at least 2 h (Fig. 1g). This is not the case for volcanic ash events that occurred in June 2020 (Event 1) and April 2021 (Event 3); as those were considered minor events and most volcanic ashes fly nearby the Pacific coast. Thus, $PM_{2.5}$ measurements showed the volcanic plume ash intensity was greater in September 2020, than it was in June 2020, which was greater or equal to April 2021. Since seasonality differs from year to year, the presented observations may change with changes in the rain pattern. Hence, during the absence of rain, it is most likely that volcanic ashes may be transported to the city during the wet season as well. For instance, there is evidence of long-range transport of African dust reaching the Brazilian Amazon basin during the wet season (Jan–May) (Moran-Zuloaga et al. 2018; Pöhlker et al. 2018).

On September 20, 2020 (Event 2) during the dry season, vertical profile data showed that there was a mix of smoke, polluted dust, and dust mainly allocated at 5 km height as presented in Fig. 4b. This volcanic plume was well described by Bernard et al. (2022) by using MAX-DOAS. Vertical profiles on Event 1 and Event 3 were marked by the influence of clean marine and continental pollution.

Preliminary analysis using HYSPLIT provides an approximation of the volcanic plume events, but as mentioned by Tadini et al. (2020), a standalone HYSPLIT analysis does not account for complex settling mechanisms of volcanic ash. Therefore, air masses trajectories with OMI maps (Saturno et al. 2018) and other models (Williams et al. 2019; Tadini et al. 2022) help to minimize uncertainties in the model and dispersive processes in the atmosphere.

Computational models are very resourceful tools to visualize patterns at regional scales of volcanic dispersion (Parra et al. 2016; Bernard et al. 2022; Vasconez et al. 2022). However, they need to be correlated with ground measurements, particularly with fine-mode particles as described by Wang et al. (2016) on coarse-mode and fine-mode aerosol particles. The more complex model decreased the bias but increases the variance (De'ath 2007). A good correlation agreement between ground measurements and satellite data was mentioned by McCormick et al. (2014) during the Tungurahua volcanic plume in 2016. Therefore, when meteorological conditions are favorable, natural or anthropogenic pollutants are easily available by long-range transport of dust (Wang et al. 2016; Wang et al. 2023), marine spray (Makowski Giannoni et al. 2014), volcanic plumes (Carn et al. 2011; Wu et al. 2018), and biomass burning (Mendez-Espinosa et al. 2019; Holanda et al. 2020).

In addition to the analysis of air mass trajectories combined with satellite information and atmospheric aerosol concentrations, the study of ash composition is essential to understand the underlying mechanism of ash formation during explosive volcanic eruptions. Understanding such geomorphology (i.e., sharp edges and large solids) can help mitigate the dangers the ash presents as it is displaced into more populated areas. These risks include harmful health effects on the population. Considering that volcanic ash particles varied in size and shape, and they have a unique fragmentation and transport process as mentioned by Mulas et al. (2019), higher concentrations of $PM_{2.5}$ from volcanic origins can cause serious respiratory issues at higher concentrations (Beckett 2000; Pöschl 2005), particularly in the elderly and children (Horwell 2007).

The present study provides information regarding volcanic ashes deposited in Guayaquil. For volcanic ashes corresponding to $PM_{2.5}$, they were prone to reach the city during periods when rain was absent. Other external factors seem related to the transport of macro particles, those bigger than 30 µm. From the data gathered in this study, it is assumed that the force of each eruption is directly linked with the meteorological conditions (refer to Fig. S5). Nonetheless, more research, particularly of those particles is needed to better understand macro particle transport.

The ash particle of the June 2020 eruption exhibits two types: (i) dark-colored glass, low crystallinity, well-roundedness, rounded 2–4 µm-sized vesicles (Fig. 5a) and (ii) light-colored, angular, low vesicles/amygdaloids shape, and low roundness with 100 µm-sized vesicles (Fig. 5b). The ash particles of September 2020 exhibit a light-colored contrast as mentioned by Bernard et al. (2022), with angular to spherical (Fig. 5c) to elongated (Fig. 5d) low roundness with vesicles of about 10 µm. The ash particles that erupted in April 2021 are quite similar to the ash particle of September 2020. According to Malek et al. (2019), volcanic

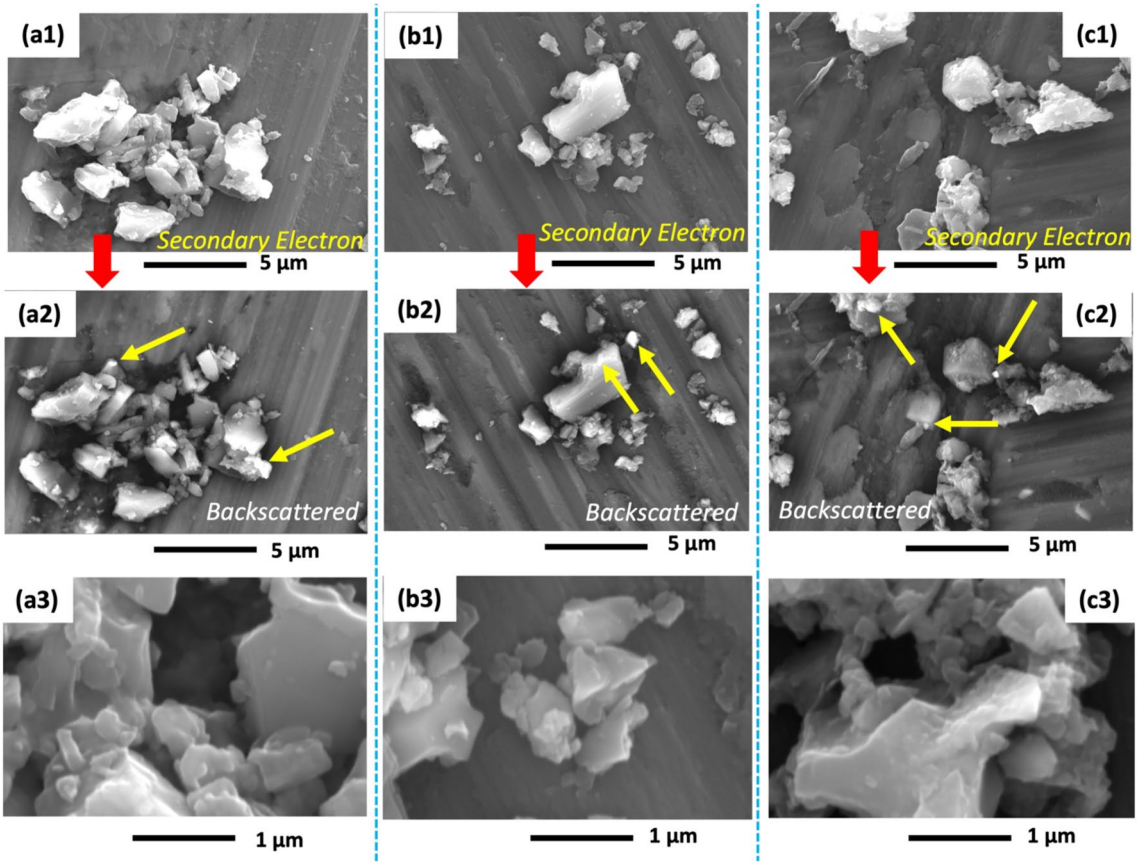

Fig. 9 (a1-a2) Ashes from the volcanic eruption in June 2020; (b1-b3) Ashes from the volcanic eruption in September 2020; and (c1-c3) Ashes from the volcanic eruption in April 2021. SEM images (a2), (b2), and (c3) are from backscattered electron SEM. The SEM images (a3), (b3), and (c3) are higher resolution images revealing the small size of the fine grain structures

ashes with flat surfaces were more aerodynamic and prone to long-range transport. In the present study, larger particles (> 10 µm) and finer particles (< 2 µm) with a variety of shapes including flat surfaces were found. These findings agree with Eychenne and Engwell (2022), which described bimodal fall deposits that were formed after a strong eruption with particle sizes below 100 µm and grain-size decay with distance from the source that can be related to eruption plume height and intensity.

The SEM-EDX chemical characterization of selected samples of volcanic ashes of the Sangay revealed that they are composed of three major chemical species (Figs. 6, 7, and 8). This includes C (4%), O (11%), and Si (6%), and it was found to be similar proportion during the three eruption events. As previously presented in the results, EDX spectra collected on the fine-grain materials contain peaks of carbon. That is, the carbon peak is present in the sample analysis for all three events. It is important to note that the methodology used herein does not allow us to confirm nor deny that carbon corresponds exclusively from the volcanic explosion, since long-range transport and atmospheric conditions may interfere during the dry deposition (Seinfeld and Pandis 1998; Ayris and Delmelle 2012; Trejos et al. 2021) (Fig. S4). Nonetheless, there is evidence of carbon found in volcanic ashes as reported by Malek et al. (2019). Furthermore, other minor chemical species are present in the samples, including Na (0.1%), Mg (0.3%), Al (70%), P (2%), Ca (1%), S (0.3%), and Fe (0.6%), respectively. It also reveals that the elemental composition is similar to the structure size. For instance, in the sample of September 2020, the particle for point (1) in Fig. 7(c1) has a size of approximately 8 µm while the particle for point (4) is only a few micrometers (Fig. 7(c4)) and both have similar composition. Chemical elements such as Al, Si, and Fe composition of the Nevado de Ruiz volcano (Trejos et al. 2021) and Grímsvötn volcano (Lieke et al. 2013) were the same as in the present study.

The SEM backscatter electron images of the ashes support our EDX results in that the structures appear uniform or well-mixed (Fig. 9). The SEM image in Fig. 9(a1) is obtained from secondary electrons originating from or near the surface regions of the sample from the June 2020 eruption. In contrast, the black and white SEM image in Fig. 9(a2) is a backscattered electron (BSE) image of the same region. Figure 9(b1–b2) and Fig. 9(c1–c2) represent

secondary and electron images from sample ashes collected in September 2020 and April 2021, respectively. Through a comparison of the SEM backscattered electron images for the samples studied, it can be observed that the surface holding the samples is a single dark contrast. It is also evident that most of the surface of fragments Fig. 9a2, b2, c2 do not have very significant contrast supporting our EDX results that the samples appear to be well mixed. Although, it can be observed from the backscattered electron images that on the surface of some of the structures there are smaller structures that have a very different contrast (very bright as pointed out by the arrows) under the electron beam suggesting that they are of a different material than the relatively larger particles. The well-mixed elements forming the fragments can be explained by the mixing enthalpy between the elements and the melting points of the elements in such a harsh volcanic environment. The higher resolution SEM images in Fig. 9(a3, b3, c3) shows the relatively small size of the fine structures.

From ratio images, the present study found more coarse mode particles on observations done by Bernard et al. (2022); in which, coarse particles correspond to core sediment (heavier particles) while fine mode (lighter particles) correspond to ash clouds. This may explain there were more coarse mode and some fine mode particles (from 2.5 µm or smaller) as presented in Figs. 6, 7, 8, and 9; and the ground measurement of $PM_{2.5}$ peaks during volcanic plumes in Fig. 1g.

Once the volcanic ashes were deposited from the ecosystem perspective, open activities like agriculture, aquaculture, and trade markets are immediately affected due to the ash's sediments (Wilson et al. 2011) and soil amendments (Minasny et al. 2021). Considering those are natural events, it is important to consider the ecosystem recovery in the long-term (Fiantis et al. 2019). Since the Andes Mountains are surrounded by volcanoes, volcanic ash depositions are part of the natural ecosystems in Ecuador and Colombia's northwest continent. These volcanic events diminished human settlements over the region as mentioned by Lim et al. (2014). Finally, we can infer that air quality can be significantly altered due to the volcanic ashes suspended in the air for an extended period, which may produce detrimental effects on the inhabitants nearby the volcano and further away near the coastal areas (Plumlee et al. 2014; Stewart et al. 2021). The higher concentrations of fine particles $PM_{2.5}$ ($PM < 2.5$ µm) and sharp shapes produced by the volcanic ashes may affect the respiratory system of nearby residents (Pöschl 2005; Tang et al. 2020).

Sangay volcanic plume ashes are a constant threat to the population due to sporadic emissions and it needs to be monitored and complemented by remote sensing tools supported in situ measurements to understand the volcanic ash dispersion and deposition (Sangay volcano and many others, refer to Table S1). Hence, SO_2 total mass column was higher during the transitional and dry seasons in comparison to the wet season, as the same for AOD 550 nm, all of them during the volcanic events which corroborates our findings. In summary, the present study demonstrates the importance of meteorological stations coupled with $PM_{2.5}$ sensors that can help provide sensitive information on pollutants. Moreover, the present work demonstrated the importance of the study of volcanic ashes from the regional to the microscopic perspective.

Conclusions

The present study emphasizes the importance of continuous $PM_{2.5}$ ground measurements in Guayaquil despite the fact of using a low-cost instrument. Although there are some limitations, the adequate use of meteorological, $PM_{2.5}$, and satellite maps, and data helped to monitor aerosols concentrations, to quantify the impact of Sangay volcanic plumes on the air quality in the city of Guayaquil, and to visualize their path and the conditions determining the dispersion of the volcanic aerosols. By doing this, it was found that the wet and the transitional seasons usually are cleaner periods (monthly average values of 6 ± 2 µg m^{-3}) because of wet scavenging, whereas the mean average $PM_{2.5}$ may reach monthly average values of 16 ± 3 µg m^{-3} during the dry season of 2020. These values may substantially increase up to 133 ± 40 µg m^{-3}; independently of the season when the volcano emissions occur in the absence of rainfall and coinciding with a period of high wind speeds and wind directions from the emissions source to the coast. The present study evidence that the reachability of volcanic ashes is closely related to their eruption force, meteorological conditions, and the predisposition to facilitate long-range transport.

The grain size analysis of the Sangay ashes deposited illustrated a double hump shape, one hump at a median of 3 to 4 µm (close to $PM_{2.5}$ measured in this study), and a second hump with a median of 60 to 70 µm (large particles). The present study reveals that an intense volcanic eruption easily transports large particles (100 µm), and breathable particles underlie the $PM_{2.5}$ scope. Regarding the ash morphology, there were found round and spherical shapes for particles bigger than 10 µm while some fragmented and sharp edges for those particles below 2.5 µm. Moreover, the morphology of the finer ash particles has a spherical-like shape, sharp edges, and many have an irregular shape. Moreover, EDX analysis showed that Sangay ashes were mainly composed of C, O, Si, Mg, Al, Ca, and Fe while P and Ti were found in small proportions, and not in all the analyzed samples. It is important to state that more in-depth studies are needed to better understand the physical factors and source origins

of those particles, and a more conspicuous study about the nature and the composition.

In summary, the results of this study provide a brief examination of volcanic events that provides sensitive information during long-range transport dispersion occurring in 2020 and 2021 and provide a brief overview of the Sangay volcano ashes morphology and composition; to be considered by local government and local communities during future volcanic events in the region.

Supplementary Information The online version contains supplementary material available at https://doi.org/10.1007/s11869-023-01434-w.

Acknowledgements We would like to thank Christopher Pöhlker, David Walter, MPIC, and ATTO project staff for their advice and fruitful collaborations. DMZ acknowledges the support of the Bundesministerium für Bildung und Forschung (BMBF contract 01LB1001A). ERC was supported by the Ramon y Cajal fellowship (RYC2020-030762-I), the CRUST R-Forze (PID2021-127631NA-I00) founded by FEDER/Ministerio de Ciencia e Inovación-Agencia Estatal de investigación and the European Union Funds for Regional Development and the project (PPUENTE2022/003) founded by the University of Almeria (Plan propio de Investigacion). We would like to thank Mauricio Cornejo, Julio Cáceres, Héctor Ayon from ESPOL, Stanislaus Sonnenholzner from CENAIM, and Paola Ochoa from ESPAE; Fernando Ayala, Gustavo González from Benemérito Cuerpo de Bomberos de Guayaquil, María Fernanda Rumbea, and Verónica Navarrete from Dirección de Ambiente, Sostenibilidad y Cambio Climático of the Municipalidad de Guayaquil. Many thanks to David Carslaw and R Core team for supporting the open software community, and J.A. Huffman for the igor scripts. The authors gratefully acknowledge the NOOA Air Resources Laboratory (ARL) for the provision of the HYSPLIT transport and dispersion model and/or READY website (https://www.arl.nooa.gov/ready.php, last access: 2022-04-15) used in this publication. We acknowledge the team from NASA Giovanni (Geospatial Interactive Online Visualization and Analyze Infrastructure). The data was taken from the following website https://giovanni.gsfc.nasa.gov/giovanni/, for downloading products from GDAS, MODIS, MERRA, and OMI, last visited on March 30, 2022. The CALIPSO datasets were consulted on https://www-calipso.larc.nasa.gov/tools/data_avail/, last visited on April 16, 2022. Sentinel 5 Precursor TROPOMI level 2 product (http://www.tropomi.eu/data-products/ last access: 2022-04-19) developed with funding from the Netherland Space Office (NSO) and processed with funding from the European Space Agency (ESA). We would like to thank the National Aeronautics and Space Administration NASA for the vertical profiles from the Cloud-Aerosol Lidar and Infrared Pathfinder Satellite Observations (CALIPSO) from https://www-calipso.larc.nasa.gov/tools/data_avail/, last visited on April 16, 2022. We would like to thank the Volcano Monitoring System powered by Sentinel satellites (1, 2, 5P) and AI from http://www.mounts-project.com/home, last visited: April 27, 2023. WMM would like to thank Dr. Preston Larson from the SRNEML at the University of Oklahoma for providing technical and helpful discussions with SEM studies. WMM would like to acknowledge the support of the Cluster SEED Funding by the School of Aerospace and Mechanical Engineering at the University of Oklahoma.

Author contribution DMZ, WMM, and MM design and formulate the initial research proposal. DMZ, WMM, ERC, and PH conceptualized the measurements, the logistics, and the funds. MM collected the field samples. DMZ and WMM conducted microscopy studies of the fine-sized ash samples. ERC, DMZ, and PH assisted with the remote sensing and statistical analysis. All the authors read and approved the content of the manuscript.

Funding Open Access funding enabled and organized by Projekt DEAL. Open Access funding enables and organized by Projekt DEAL through Johannes Gutenberg University from DMZ.

Data availability The data presented in Fig. 1 will be available to the Edmond data repository at the following link: https://doi.org/10.17617/3.UA3GQG. For further requests, please refer to the corresponding authors.

Declarations

Ethics approval This declaration does not apply to this study.

Consent to participate This declaration does not apply to this study.

Consent for publication This declaration does not apply to this study.

Conflict of interest The authors declare no competing interests.

References

Acker J, Soebiyanto R, Kiang R, Kempler S (2014) Use of the NASA Giovanni data system for geospatial public health research: example of weather-influenza connection. ISPRS Int Geo-Inf 3(4):1372–1386. https://doi.org/10.3390/ijgi3041372

Andreae MO (2007) Aerosols before pollution. Science 315(5808):50. https://doi.org/10.1126/science.1136529

Ayris PM, Delmelle P (2012) The immediate environmental effects of tephra emission. Bull Volcanol 74(9):1905–1936. https://doi.org/10.1007/s00445-012-0654-5

Beckett WS (2000) Occupational respiratory diseases. N Engl J Med 342(6):406–413. https://doi.org/10.1056/NEJM200002103420607

Bernard B, Samaniego P, Mastin L, Hernandez S, Pino G, Kibler J, Encalada M, Hidalgo S, Vizuete N (2022) Forecasting and communicating the dispersion and fallout of ash during volcanic eruptions: lessons from the September 20, 2020 eruptive pulse at Sangay volcano Ecuador. Front Earth Sci 10:912835

Bonadonna C, Houghton BF (2005) Total grain-size distribution and volume of tephra-fall deposits. Bull Volcanol 67(5):441–456. https://doi.org/10.1007/s00445-004-0386-2

Cañadas Cruz LC (1983) El mapa bioclimático y ecológico del Ecuador. Banco Central del Ecuador

Carn SA, Froyd KD, Anderson BE, Wennberg P, Crounse J, Spencer K, Dibb JE, Krotkov NA, Browell EV, Hair JW, Diskin G, Sachse G, Vay SA (2011) In situ measurements of tropospheric volcanic plumes in Ecuador and Colombia during TC4. J Geophys Res-Atmos 116(D10). https://doi.org/10.1029/2010jd014718

Carn SA, Krueger AJ, Arellano S, Krotkov NA, Yang K (2008) Daily monitoring of Ecuadorian volcanic degassing from space. J

Volcanol Geotherm Res 176(1):141–150. https://doi.org/10.1016/j.jvolgeores.2008.01.029
Carslaw DC, Beevers SD (2013) Characterising and understanding emission sources using bivariate polar plots and k-means clustering. Environ Model Softw 40:325–329. https://doi.org/10.1016/j.envsoft.2012.09.005
Carslaw DC, Ropkins K (2012) Openair - an R package for air quality data analysis. Environ Model Softw 27-28:52–61. https://doi.org/10.1016/j.envsoft.2011.09.008
Cioni R, Tadini A, Gurioli L, Bertagnini A, Mulas M, Bevilacqua A, Neri A (2020) Estimating eruptive parameters and related uncertainties for pyroclastic density currents deposits: worked examples from Somma-Vesuvius (Italy). Bull Volcanol 82(9):65. https://doi.org/10.1007/s00445-020-01402-7
Crutzen PJ (2021) We live in the anthropocene, so will our grandchildren. Her Russ Acad Sci 91(1):13–16. https://doi.org/10.1134/S1019331621010020
De'ath G (2007) Boosted trees for ecological modeling and prediction. Ecology 88(1):243–251. https://doi.org/10.1890/0012-9658(2007)88[243:btfema]2.0.co;2
Draxler R, Barbara S, Rolph G, Ariel S, Albion T (2018) HYSPLIT4 user's guide. National Oceanic and Atmospheric Administration
Engwell S, Eychenne J (2016) Contribution of fine ash to the atmosphere from plumes associated with pyroclastic density currents. In: Cashman K, Ricketts H, Rust A, Watson M (eds) Mackie S. Elsevier, Volcanic Ash, pp 67–85. https://doi.org/10.1016/b978-0-08-100405-0.00007-0
Eychenne J, Engwell SL (2022) The grainsize of volcanic fall deposits: spatial trends and physical controls. Geol Soc Am Bull. https://doi.org/10.1130/B36275.1
Fiantis D, Ginting FI, Gusnidar NM, Minasny B (2019) Volcanic ash, insecurity for the people but securing fertile soil for the future. Sustainability 11(11):3072
Fioletov V, Mclinden CA, Griffin D, Theys N, Loyola DG, Hedelt P, Krotkov NA, Li C (2020) Anthropogenic and volcanic point source SO2 emissions derived from TROPOMI on board Sentinel-5 Precursor: first results. Atmos Chem Phys 20(9):5591–5607. https://doi.org/10.5194/acp-20-5591-2020
Foken T, Beyrich F, Wulfmeyer V (2021) Introduction to atmospheric measurements. In: Foken T (ed) Springer handbook of atmospheric measurements. Springer Handbooks. Springer International Publishing, Cham, pp 3–31. https://doi.org/10.1007/978-3-030-52171-4_1
Folk RL (1980) Petrology of sedimentary rocks. Hemphill Publishing Company, Austin, Texas
Forbes L, Jarvis D, Potts J, Baxter PJ (2003) Volcanic ash and respiratory symptoms in children on the island of Montserrat. British West Indies Occup Environ Med 60(3):207–211. https://doi.org/10.1136/oem.60.3.207
Gaunt HE, Bernard B, Hidalgo S, Proano A, Wright H, Mothes P, Criollo E, Kueppers U (2016) Juvenile magma recognition and eruptive dynamics inferred from the analysis of ash time series: the 2015 reawakening of Cotopaxi volcano. J Volcanol Geotherm Res 328:134–146. https://doi.org/10.1016/j.jvolgeores.2016.10.013
Genareau K, Mulukutla GK, Proussevitch AA, Durant AJ, Rose WI, Sahagian DL (2013) The size range of bubbles that produce ash during explosive volcanic eruptions. J Appl Volcanol 2(1):4. https://doi.org/10.1186/2191-5040-2-4
Gislason SR, Hassenkam T, Nedel S, Bovet N, Eiriksdottir ES, Alfredsson HA, Hem CP, Balogh ZI, Dideriksen K, Oskarsson N, Sigfusson B, Larsen G, Stipp SL (2011) Characterization of Eyjafjallajokull volcanic ash particles and a protocol for rapid risk assessment. Proc Natl Acad Sci U S A 108(18):7307–7312. https://doi.org/10.1073/pnas.1015053108
Gorelick N, Hancher M, Dixon M, Ilyushchenko S, Thau D, Moore R (2017) Google Earth Engine: planetary-scale geospatial analysis for everyone. Remote Sens Environ 202:18–27. https://doi.org/10.1016/j.rse.2017.06.031
Hamilton DS, Perron MMG, Bond TC, Bowie AR, Buchholz RR, Guieu C, Ito A, Maenhaut W, Myriokefalitakis S, Olgun N, Rathod SD, Schepanski K, Tagliabue A, Wagner R, Mahowald NM (2022) Earth, wind, fire, and pollution: aerosol nutrient sources and impacts on ocean biogeochemistry. Annu Rev Mar Sci 14(1):303–330. https://doi.org/10.1146/annurev-marine-031921-013612
Holanda BA, Pöhlker ML, Walter D, Saturno J, Sörgel M, Ditas J, Ditas F, Schulz C, Franco MA, Wang Q, Donth T, Artaxo P, Barbosa HMJ, Borrmann S, Braga R, Brito J, Cheng Y, Dollner M, Kaiser JW et al (2020) Influx of African biomass burning aerosol during the Amazonian dry season through layered transatlantic transport of black carbon-rich smoke. Atmos Chem Phys 20(8):4757–4785. https://doi.org/10.5194/acp-20-4757-2020
Horwell C (2007) Grain size analysis of volcanic ash for the rapid assessment of respiratory health hazard. Journal of environmental monitoring : JEM 9:1107–1115. https://doi.org/10.1039/B710583P
Kassambara A (2017) Practical guide to cluster analysis in R: unsupervised machine learning.
Langmann B (2013) Volcanic ash versus mineral dust: atmospheric processing and environmental and climate impacts. ISRN Atmos Sci 2013:245076. https://doi.org/10.1155/2013/245076
Le Pennec J-L, Ruiz GA, Ramón P, Palacios E, Mothes P, Yepes H (2012) Impact of tephra falls on Andean communities: the influences of eruption size and weather conditions during the 1999–2001 activity of Tungurahua volcano, Ecuador. J Volcanol Geotherm Res 217-218:91–103. https://doi.org/10.1016/j.jvolgeores.2011.06.011
Lelieveld J, Evans JS, Fnais M, Giannadaki D, Pozzer A (2015) The contribution of outdoor air pollution sources to premature mortality on a global scale. Nature 525(7569):367–371. https://doi.org/10.1038/nature15371
Lettino A, Caggiano R, Fiore S, Macchiato M, Sabia S, Trippetta S (2012) Eyjafjallajökull volcanic ash in southern Italy. Atmos Environ 48:97–103. https://doi.org/10.1016/j.atmosenv.2011.05.037
Lieke KI, Kristensen TB, Korsholm US, Sørensen JH, Kandler K, Weinbruch S, Ceburnis D, Ovadnevaite J, O'Dowd CD, Bilde M (2013) Characterization of volcanic ash from the 2011 Grímsvötn eruption by means of single-particle analysis. Atmos Environ 79:411–420. https://doi.org/10.1016/j.atmosenv.2013.06.044
Lim S, Ledru M-P, Valdez F, Devillers B, Houngnon A, Favier C, Bremond L (2014) Ecological effects of natural hazards and human activities on the Ecuadorian Pacific coast during the late Holocene. Palaeogeogr Palaeoclimatol Palaeoecol 415:197–209. https://doi.org/10.1016/j.palaeo.2013.12.021
Liu EJ, Cashman KV, Rust AC, Gislason SR (2015) The role of bubbles in generating fine ash during hydromagmatic eruptions. Geology 43(3):239–242. https://doi.org/10.1130/G36336.1
Liu EJ, Oliva M, Antoniades D, Giralt S, Granados I, Pla-Rabes S, Toro M, Geyer A (2016) Expanding the tephrostratigraphical framework for the South Shetland Islands, Antarctica, by combining compositional and textural tephra characterisation. Sediment Geol 340:49–61. https://doi.org/10.1016/j.sedgeo.2015.08.002
Makowski Giannoni S, Rollenbeck R, Trachte K, Bendix J (2014) Natural or anthropogenic? On the origin of atmospheric sulfate deposition in the Andes of southeastern Ecuador. Atmos Chem Phys 14(20):11297–11312. https://doi.org/10.5194/acp-14-11297-2014
Malek MA, Eom H-J, Hwang H, Hur SD, Hong S, Hou S, Ro C-U (2019) Single particle mineralogy of microparticles from Himalayan ice-cores using SEM/EDX and ATR-FTIR imaging techniques for identification of volcanic ash signatures. Chem Geol 504:205–215. https://doi.org/10.1016/j.chemgeo.2018.11.010

Markus B, Valade S, Wöllhaf M, Hellwich O (2023) Automatic retrieval of volcanic SO2 emission source from TROPOMI products. Front Earth Sci 10. https://doi.org/10.3389/feart.2022.1064171

McCormick BT, Herzog M, Yang J, Edmonds M, Mather TA, Carn SA, Hidalgo S, Langmann B (2014) A comparison of satellite- and ground-based measurements of SO2 emissions from Tungurahua volcano Ecuador. J Geophys Res Atmos 119(7):4264–4285. https://doi.org/10.1002/2013JD019771

McCormick MP, Thomason LW, Trepte CR (1995) Atmospheric effects of the Mt Pinatubo eruption. Nature 373(6513):399–404. https://doi.org/10.1038/373399a0

Mendez-Espinosa JF, Belalcazar LC, Morales Betancourt R (2019) Regional air quality impact of northern South America biomass burning emissions. Atmos Environ 203:131–140. https://doi.org/10.1016/j.atmosenv.2019.01.042

Mills OP, Rose WI (2010) Shape and surface area measurements using scanning electron microscope stereo-pair images of volcanic ash particles. Geosphere 6(6):805–811. https://doi.org/10.1130/GES00558.1

Minasny B, Fiantis D, Hairiah K, Van Noordwijk M (2021) Applying volcanic ash to croplands – the untapped natural solution. Soil Security 3:100006. https://doi.org/10.1016/j.soisec.2021.100006

Moran-Zuloaga D, Ditas F, Walter D, Saturno J, Brito J, Carbone S, Chi X, Hrabě de Angelis I, Baars H, Godoi RHM, Heese B, Holanda BA, Lavrič JV, Martin ST, Ming J, Pöhlker ML, Ruckteschler N, Su H, Wang Y et al (2018) Long-term study on coarse mode aerosols in the Amazon rain forest with the frequent intrusion of Saharan dust plumes. Atmos Chem Phys 18(13):10055–10088. https://doi.org/10.5194/acp-18-10055-2018

Moran-Zuloaga D, Merchan-Merchan W, Rodríguez-Caballero E, Hernick P, Cáceres J, Cornejo MH (2021) Overview and seasonality of PM10 and PM2.5 in Guayaquil, Ecuador. Aerosol Sci Eng. https://doi.org/10.1007/s41810-021-00117-2

Mulas M, Chunga K, Garcés D, Escobar Segovia K (2019) Sedimentological study of distal rain-triggered lahars: the case of West Coast of Ecuador. Latin Am J Sedimentol Basin Anal 26:32

Oyola P, Carbone S, Timonen H, Torkmahalleh M, Linden J (2022) Editorial: rise of low-cost sensors and citizen science in air quality studies. Front Environ Sci 10. https://doi.org/10.3389/fenvs.2022.868543

Parra R, Bernard B, Narváez D, Le Pennec J-L, Hasselle N, Folch A (2016) Eruption source parameters for forecasting ash dispersion and deposition from vulcanian eruptions at Tungurahua volcano: insights from field data from the July 2013 eruption. J Volcanol Geotherm Res 309:1–13. https://doi.org/10.1016/j.jvolgeores.2015.11.001

Plumlee GS, Morman SA, Meeker GP, Hoefen TM, Hageman PL, Wolf RE (2014) 11.7 - The environmental and medical geochemistry of potentially hazardous materials produced by disasters. In: Holland HD, Turekian KK (eds) Treatise on geochemistry, 2nd edn, Elsevier, Oxford, pp 257–304. https://doi.org/10.1016/B978-0-08-095975-7.00907-4

Pöhlker C, Walter D, Paulsen H, Könemann T, Rodríguez-Caballero E, Moran-Zuloaga D, Brito J, Carbone S, Degrendele C, Després VR, Ditas F, Holanda BA, Kaiser JW, Lammel G, Lavrič JV, Ming J, Pickersgill D, Pöhlker ML, Praß M et al (2019) Land cover and its transformation in the backward trajectory footprint region of the Amazon Tall Tower Observatory. Atmos Chem Phys 19(13):8425–8470. https://doi.org/10.5194/acp-19-8425-2019

Pöhlker ML, Ditas F, Saturno J, Klimach T, Hrabě de Angelis I, Araùjo AC, Brito J, Carbone S, Cheng Y, Chi X, Ditz R, Gunthe SS, Holanda BA, Kandler K, Kesselmeier J, Könemann T, Krüger OO, Lavrič JV, Martin ST et al (2018) Long-term observations of cloud condensation nuclei over the Amazon rain forest – Part 2: Variability and characteristics of biomass burning, long-range transport, and pristine rain forest aerosols. Atmos Chem Phys 18(14):10289–10331. https://doi.org/10.5194/acp-18-10289-2018

Pohlker ML, Kruger OO, Forster J-D, Elbert W, Frohlich-Nowoisky J, Poschl U, Pohlker C, Bagheri G, Bodenschatz E, Huffman JA, Scheithauer S, Mikhailov E (2021) Respiratory aerosols and droplets in the transmission of infectious diseases. arXiv preprint arXiv 2103:01188. https://doi.org/10.48550/arXiv.2103.01188

Pompilio M, Bertagnini A, Del Carlo P, Di Roberto A (2017) Magma dynamics within a basaltic conduit revealed by textural and compositional features of erupted ash: the December 2015 Mt Etna paroxysms. Sci Rep 7(1):4805. https://doi.org/10.1038/s41598-017-05065-x

Pöschl U (2005) Atmospheric aerosols: composition, transformation, climate and health effects. Angew Chem Int Ed 44(46):7520–7540

R Development Core Team (2021) R: a language and environment for statistical computing. R Foundation for Statistical Computing, Vienna, Austria. https://doi.org/https://www.r-project.org/

Ritter C, Münkel C (2021) Backscatter lidar for aerosol and cloud profiling. In: Foken T (ed) Springer handbook of atmospheric measurements. Springer International Publishing, Cham, pp 683–717. https://doi.org/10.1007/978-3-030-52171-4_24

Rolph G, Stein A, Stunder B (2017) Real-time environmental applications and display sYstem: READY. Environ Model Softw 95:210–228. https://doi.org/10.1016/j.envsoft.2017.06.025

RStudio Team (2020) RStudio: integrated development for R. RStudio, Boston, MA. http://www.rstudio.com/

Saturno J, Ditas F, Pöhkler M, Carbone S, Brito J, Holanda B, Hrabe de Angelis I, Moran-Zuloaga D, Walter D, Artaxo P, Pöschl U, Andreae MO, Pöhlker C (2018) African volcanic emission influencing the atmosphere over the Amazon rain forest (to be submitted). Atmos Chem Phys. https://doi.org/10.5194/acp-18-10391-2018

Seinfeld JH, Pandis SN (1998) Atmospheric chemistry and physics. Wiley, New York

Stein AF, Draxler RR, Rolph GD, Stunder BJB, Cohen MD, Ngan F (2015) NOAA's HYSPLIT atmospheric transport and dispersion modeling system. Bull Am Meteorol Soc 96(12):2059–2077. https://doi.org/10.1175/BAMS-D-14-00110.1

Stewart C, Damby DE, Horwell CJ, Elias T, Ilyinskaya E, Tomašek I, Longo BM, Schmidt A, Carlsen HK, Mason E, Baxter PJ, Cronin S, Witham C (2021) Volcanic air pollution and human health: recent advances and future directions. Bull Volcanol 84(1):11. https://doi.org/10.1007/s00445-021-01513-9

Tadini A, Azzaoui N, Roche O, Samaniego P, Bernard B, Bevilacqua A, Hidalgo S, Guillin A, Gouhier M (2022) Tephra fallout probabilistic hazard maps for Cotopaxi and Guagua Pichincha Volcanoes (Ecuador) with uncertainty quantification. J Geophys Res Solid Earth 127(2):e2021JB022780. https://doi.org/10.1029/2021JB022780

Tadini A, Roche O, Samaniego P, Guillin A, Azzaoui N, Gouhier M, de Michieli Vitturi M, Pardini F, Eychenne J, Bernard B, Hidalgo S, Le Pennec JL (2020) Quantifying the uncertainty of a coupled plume and tephra dispersal model: PLUME-MOM/HYSPLIT simulations applied to Andean Volcanoes. J Geophys Res : Solid Earth 125(2):e2019JB018390. https://doi.org/10.1029/2019JB018390

Tang Y, Tong DQ, Yang K, Lee P, Baker B, Crawford A, Luke W, Stein A, Campbell PC, Ring A, Flynn J, Wang Y, McQueen J, Pan L, Huang J, Stajner I (2020) Air quality impacts of the 2018 Mt. Kilauea Volcano eruption in Hawaii: a regional chemical transport model study with satellite-constrained emissions. Atmos Environ 237:117648. https://doi.org/10.1016/j.atmosenv.2020.117648

Trejos EM, Silva LFO, Hower JC, Flores EMM, González CM, Pachón JE, Aristizábal BH (2021) Volcanic emissions and atmospheric

pollution: a study of nanoparticles. Geosci Front 12(2):746–755. https://doi.org/10.1016/j.gsf.2020.08.013

Valverde V, Mothes PA, Beate B, Bernard J (2021) Enormous and far-reaching debris avalanche deposits from Sangay volcano (Ecuador): multidisciplinary study and modeling the 30 ka sector collapse. J Volcanol Geotherm Res 411:107172. https://doi.org/10.1016/j.jvolgeores.2021.107172

Vasconez FJ, Hidalgo S, Battaglia J, Hernandez S, Bernard B, Coppola D, Valade S, Ramón P, Arellano S, Liorzou C, Almeida M, Ortíz M, Córdova J, Vásconez Müller A (2022) Linking ground-based data and satellite monitoring to understand the last two decades of eruptive activity at Sangay volcano Ecuador. Bull Volcanol 84(5):49. https://doi.org/10.1007/s00445-022-01560-w

Wang Q, Saturno J, Chi X, Walter D, Lavric JV, Moran-Zuloaga D, Ditas F, Pöhlker C, Brito J, Carbone S, Artaxo P, Andreae MO (2016) Modeling investigation of light-absorbing aerosols in the Amazon Basin during the wet season. Atmos Chem Phys 16(22):14775–14794. https://doi.org/10.5194/acp-16-14775-2016

Wang X, Wang Q, Prass M, Pöhlker C, Moran-Zuloaga D, Artaxo P, Gu J, Yang N, Yang X, Tao J, Hong J, Ma N, Cheng Y, Su H, Andreae MO (2023) The export of African mineral dust across the Atlantic and its impact over the Amazon Basin. Atmos Chem Phys Discuss 2023:1–44. https://doi.org/10.5194/acp-23-9993-2023

Warnach S, Bobrowski N, Hidalgo S, Arellano S, Sihler H, Dinger F, Lübcke P, Battaglia J, Steele A, Galle B, Platt U, Wagner T (2019) Variation of the BrO/SO2 molar ratio in the plume of Tungurahua Volcano between 2007 and 2017 and its relationship to volcanic activity. Front Earth Sci 7. https://doi.org/10.3389/feart.2019.00132

Wilcox PS, Addison J, Fowell SJ, Baichtal JF, Severin K, Mann DH (2019) A new set of basaltic tephras from Southeast Alaska represent key stratigraphic markers for the late Pleistocene. Quat Res 92(1):246–256. https://doi.org/10.1017/qua.2018.154

Williams DB, Ramsey MS, Wickens DJ, Karimi B (2019) Identifying eruptive sources of drifting volcanic ash clouds using back-trajectory modeling of spaceborne thermal infrared data. Bull Volcanol 81(9):53. https://doi.org/10.1007/s00445-019-1312-y

Wilson TM, Cole JW, Stewart C, Cronin SJ, Johnston DM (2011) Ash storms: impacts of wind-remobilised volcanic ash on rural communities and agriculture following the 1991 Hudson eruption, southern Patagonia Chile. Bull Volcanol 73(3):223–239. https://doi.org/10.1007/s00445-010-0396-1

Wilson TM, Stewart C, Sword-Daniels V, Leonard GS, Johnston DM, Cole JW, Wardman J, Wilson G, Barnard ST (2012) Volcanic ash impacts on critical infrastructure. Phys Chem Earth, Parts A/B/C 45-46:5–23. https://doi.org/10.1016/j.pce.2011.06.006

Winker DM, Vaughan MA, Omar A, Hu Y, Powell KA, Liu Z, Hunt WH, Young SA (2009) Overview of the CALIPSO mission and CALIOP data processing algorithms. J Atmos Ocean Technol 26(11):2310–2323. https://doi.org/10.1175/2009JTECHA1281.1

Woodhouse MJ, Hogg AJ, Phillips JC, Sparks RSJ (2013) Interaction between volcanic plumes and wind during the 2010 Eyjafjallajökull eruption, Iceland. J Geophys Res Solid Earth 118(1):92–109. https://doi.org/10.1029/2012JB009592

Wu X, Griessbach S, Hoffmann L (2018) Long-range transport of volcanic aerosol from the 2010 Merapi tropical eruption to Antarctica. Atmos Chem Phys 18(21):15859–15877. https://doi.org/10.5194/acp-18-15859-2018

Zuo M, Zhou T, Man W, Chen X, Liu J, Liu F, Gao C (2022) Volcanoes and climate: sizing up the impact of the recent Hunga Tonga-Hunga Ha'apai volcanic eruption from a historical perspective. Adv Atmos Sci. https://doi.org/10.1007/s00376-022-2034-1